Article

SOURCE DATA | TRANSPARENT PROCESS | OPEN ACCESS

THE EMBO JOURNAL

CCR5 deficiency impairs CD4$^+$ T-cell memory responses and antigenic sensitivity through increased ceramide synthesis

Ana Martín-Leal[1,†], Raquel Blanco[1,†], Josefina Casas[2,3], María E Sáez[4], Elena Rodríguez-Bovolenta[5], Itziar de Rojas[6], Carina Drechsler[7,8,9], Luis Miguel Real[10,11], Gemma Fabrias[2,3], Agustín Ruíz[6,12], Mario Castro[13], Wolfgang WA Schamel[7,8,14], Balbino Alarcón[5], Hisse M van Santen[5] & Santos Mañes[1,*]

Abstract

CCR5 is not only a coreceptor for HIV-1 infection in CD4$^+$ T cells, but also contributes to their functional fitness. Here, we show that by limiting transcription of specific ceramide synthases, CCR5 signaling reduces ceramide levels and thereby increases T-cell antigen receptor (TCR) nanoclustering in antigen-experienced mouse and human CD4$^+$ T cells. This activity is CCR5-specific and independent of CCR5 co-stimulatory activity. CCR5-deficient mice showed reduced production of high-affinity class-switched antibodies, but only after antigen rechallenge, which implies an impaired memory CD4$^+$ T-cell response. This study identifies a CCR5 function in the generation of CD4$^+$ T-cell memory responses and establishes an antigen-independent mechanism that regulates TCR nanoclustering by altering specific lipid species.

Keywords ccr5[delta]32; humoral response; membrane phase; sphingolipid; T-cell receptor

Subject Category Immunology

DOI 10.15252/embj.2020104749 | Received 18 February 2020 | Revised 12 May 2020 | Accepted 14 May 2020

The EMBO Journal (2020) e104749

Introduction

The C-C motif chemokine receptor 5 (CCR5) is a seven-transmembrane G protein-coupled receptor (GPCR) expressed on the surface of several innate and adaptive immune cell subtypes, including effector and memory CD4$^+$ T lymphocytes (Gonzalez-Martin *et al*, 2012). CCR5 acts also a necessary coreceptor for infection by HIV-1. An HIV-resistant population served to identify a 32-bp deletion within the CCR5 coding region (*ccr5*Δ32), which yields a non-functional receptor (Blanpain *et al*, 2002). Since *ccr5*Δ32 homozygous individuals are seemingly healthy, a radical body of thought considers that CCR5 is dispensable for immune cell function.

Experimental and epidemiological evidence nonetheless indicates that CCR5 has an important role in innate and acquired immune responses. CCR5 and its ligands C-C motif ligand 3 (CCL3; also termed macrophage inflammatory protein [MIP]-1α), CCL4 (MIP-1β), CCL5 (regulated upon activation, normal T cell expressed and secreted [RANTES]), and CCL3L1 have been associated with exacerbation of chronic inflammatory and autoimmune diseases. Despite varying information due probably to ethnicity effects (Lee *et al*, 2013; Schauren *et al*, 2013), further complicated in admixed populations (Toson *et al*, 2017), epidemiological studies support the

1 Department of Immunology and Oncology, Centro Nacional de Biotecnología (CNB/CSIC), Madrid, Spain
2 Department of Biological Chemistry, Institute of Advanced Chemistry of Catalonia (IQAC-CSIC), Barcelona, Spain
3 CIBER Liver and Digestive Diseases (CIBER-EDH), Instituto de Salud Carlos III, Madrid, Spain
4 Centro Andaluz de Estudios Bioinformáticos (CAEBi), Seville, Spain
5 Department of Cell Biology and Immunology, Centro de Biología Molecular Severo Ochoa (CBMSO/CSIC), Madrid, Spain
6 Alzheimer Research Center, Memory Clinic of the Fundació ACE, Institut Català de Neurociències Aplicades, Barcelona, Spain
7 Signaling Research Centers BIOSS and CIBSS, University of Freiburg, Freiburg, Germany
8 Department of Immunology, Faculty of Biology, University of Freiburg, Freiburg, Germany
9 Institute for Pharmaceutical Sciences, University of Freiburg, Freiburg, Germany
10 Unit of Infectious Diseases and Microbiology, Hospital Universitario de Valme, Seville, Spain
11 Department of Biochemistry, Molecular Biology and Immunology, School of Medicine, Universidad de Málaga, Málaga, Spain
12 CIBER Enfermedades Neurodegenerativas (CIBERNED), Instituto de Salud Carlos III, Madrid, Spain
13 Interdisciplinary Group of Complex Systems, Escuela Técnica Superior de Ingeniería, Universidad Pontificia Comillas, Madrid, Spain
14 Centre for Chronic Immunodeficiency (CCI), University of Freiburg, Freiburg, Germany
*Corresponding author. Tel: +34 91 585 4840; Fax: +34 91 372 0493; E-mail: smanes@cnb.csic.es
†These authors contributed equally to this work.

*ccr5*Δ32 allele as a marker for good prognosis for these overreactive immune diseases (Vangelista & Vento, 2017). In contrast, *ccr5*Δ32 homozygotes are prone to fatal infections by several pathogens such as influenza, West Nile, and tick-borne encephalitis viruses (Lim & Murphy, 2011; Falcon *et al*, 2015; Ellwanger & Chies, 2019). The mechanisms by which the *ccr5*Δ32 polymorphism affects all these pathologies have usually been linked to the capacity of CCR5 to regulate leukocyte trafficking. For example, CCR5 deficiency reduces recruitment of influenza-specific memory $CD8^+$ T cells and accelerates macrophage accumulation in lung airways during virus rechallenge (Dawson *et al*, 2000; Kohlmeier *et al*, 2008); this could lead to acute severe pneumonitis, a fatal flu complication. CCR5 nonetheless has migration-independent functions that maximize T-cell activation by affecting immunological synapse (IS) formation (Molon *et al*, 2005; Floto *et al*, 2006; Franciszkiewicz *et al*, 2009) as well as T-cell transcription programs associated with cytokine production (Lillard *et al*, 2001; Camargo *et al*, 2009). CCR5 and its ligands are also critical for cell-mediated immunity to tumors and pathogens, including HIV-1 (Dolan *et al*, 2007; Ugurel *et al*, 2008; González-Martín *et al*, 2011; Bedognetti *et al*, 2013).

Whereas the role of CCR5 in T-cell priming is well established, its involvement in memory responses has not been addressed in depth. Only a single report suggested CCR5 involvement in $CD4^+$ T-cell promotion of memory $CD8^+$ T-cell generation through a migration-dependent process (Castellino *et al*, 2006). It remains unknown whether CCR5 endows memory T cells with additional properties. One such property is the elevated sensitivity of effector and memory ("antigen-experienced") $CD4^+$ and $CD8^+$ T cells to their cognate antigen compared to naïve cells (Kimachi *et al*, 1997; Kersh *et al*, 2003; Huang *et al*, 2013). This sensitivity gradient (memory ≫ effector > naïve) in $CD8^+$ T cells is linked to increased valency of preformed T-cell antigen receptor (TCR) oligomers at the cell surface, termed TCR nanoclusters (Kumar *et al*, 2011). This antigen-independent TCR nanoclustering (Schamel *et al*, 2005, 2006; Lillemeier *et al*, 2010; Sherman *et al*, 2011; Schamel & Alarcon, 2013) enhances antigenic sensitivity by increasing avidity to multimeric peptide-major histocompatibility complexes (Kumar *et al*, 2011; Molnar *et al*, 2012) and by allowing cooperativity between TCR molecules (Martínez-Martín *et al*, 2009; Martín-Blanco *et al*, 2018). TCRβ subunit interaction with cholesterol (Chol) and the presence of sphingomyelins (SM) are both essential for TCR nanoclustering (Molnar *et al*, 2012; Beck-Garcia *et al*, 2015). Replacement of Chol by Chol sulfate impedes TCR nanocluster formation and reduces $CD4^+CD8^+$ thymocyte sensitivity to weak antigenic peptides (Wang *et al*, 2016). Whether antigen-experienced $CD4^+$ T-cell sensitivity is linked to TCR nanoscopic organization and the homeostatic factors that regulate TCR nanoclustering remains unexplored.

Given its co-stimulatory role in $CD4^+$ T cells, we speculated that CCR5 signals would affect the antigenic sensitivity of $CD4^+$ memory T cells. To test this hypothesis, we analyzed the function of *in vivo*-generated memory $CD4^+$ T cells in wild-type (WT) and $CCR5^{-/-}$ mice, and the effect of CCR5 deficiency on CD4 T-cell help in the T-dependent humoral response. We found that CCR5 is necessary for the establishment of a functional CD4 memory response through a mechanism independent of its co-stimulatory role for the TCR signal. We show that CCR5 deficiency does not affect memory CD4 T-cell generation, but reduces their sensitivity to antigen. Our data demonstrate an unreported CCR5 regulatory role in memory $CD4^+$ T-cell function by inhibiting the synthesis of ceramides, which are identified here as negative membrane regulators of TCR nanoscopic organization.

Results

CCR5 deficiency impairs the $CD4^+$ T-cell memory response

To determine the role of CCR5 in $CD4^+$ memory T-cell generation and/or function, we adoptively transferred congenic CD45.1 mice with lymph node/spleen cell suspensions from OT-II WT or $CCR5^{-/-}$ mice (CD45.2) and subsequently infected them with OVA-encoding vaccinia virus; 5 weeks post-immunization, we analyzed spleen $CD45.2^+$ donor cells from OT-II mice. CCR5 expression on OT-II cells affected neither the total number of memory $CD4^+$ T cells (Fig 1A and B) nor the percentage of $CD4^+$ T_{EM} ($CD44^{hi}$; $CD62L^-$; Fig 1C) or T_{CM} ($CD44^{hi}$; $CD62L^+$; Fig 1D) cells generated. OT-II WT cells nonetheless had stronger responses to antigenic restimulation than OT-II $CCR5^{-/-}$ memory T cells, as determined by the percentage of interferon (IFN)γ-producing cells after *ex vivo* stimulation with $OVA_{323–339}$ (Fig 1E).

We also studied T cell-dependent B-cell responses in WT and $CCR5^{-/-}$ mice after immunization with the hapten 4-hydroxy-3-iodo-5-nitrophenylacetyl coupled to ovalbumin (NIP-OVA; Fig 1F). We detected no difference in the percentage or absolute number of T follicular helper (T_{fh}) cells ($CD4^+$, $CD44^{hi}$, $CXCR5^+$, $PD1^+$) between WT and $CCR5^{-/-}$ mice at 7 days post-immunization (Fig 1G–I). At day 30, half of the mice were boosted with the same NIP-OVA immunogen (OVA/OVA) and the other half received NIP conjugated with another carrier protein (OVA/KLH); levels of NIP-specific high- and low-affinity immunoglobulins (Ig) were analyzed 15 days later. Comparison of the humoral responses between OVA/OVA- and OVA/KLH-immunized mice would assess the effect of memory $CD4^+$ T cells specific for the first carrier protein on the humoral response to NIP. There were no differences in high/low-affinity NIP-specific IgM production between WT and $CCR5^{-/-}$ mice with either immunization strategy (Fig 1J and K). CCR5 deficiency markedly impaired the generation of high-affinity class-switched anti-NIP antibodies specifically in OVA/OVA-immunized mice (Fig 1J and K). Since class switching was similar in WT and $CCR5^{-/-}$ OVA/KLH-immunized mice, our results suggest that CCR5 deficiency reduces the generation of high-affinity class-switched immunoglobulins due to deficient memory $CD4^+$ T-cell function.

The CCR5 effect on antigen-experienced $CD4^+$ T cells is cell-autonomous

To test whether the *in vivo* memory defect associated with CCR5 deficiency was intrinsic to $CD4^+$ T cells, we activated OT-II WT and $CCR5^{-/-}$ spleen T cells with $OVA_{323–339}$ antigen for 3 days; after antigen removal, we cultured cells with IL-2 or IL-15. OT-II cells that differentiated in exogenous IL-2 expressed CCL3, CCL4, CCL5, and a functional CCR5 receptor, as determined by their ability to flux Ca^{2+} and migrate after CCL4 stimulation (Appendix Fig S1A–D).

Like $CD8^+$ T cells (Richer *et al*, 2015), OT-II cells cultured with IL-15 showed a memory-like phenotype (Fig EV1); they were smaller than IL-2-cultured cells and retained CD62L with reduced

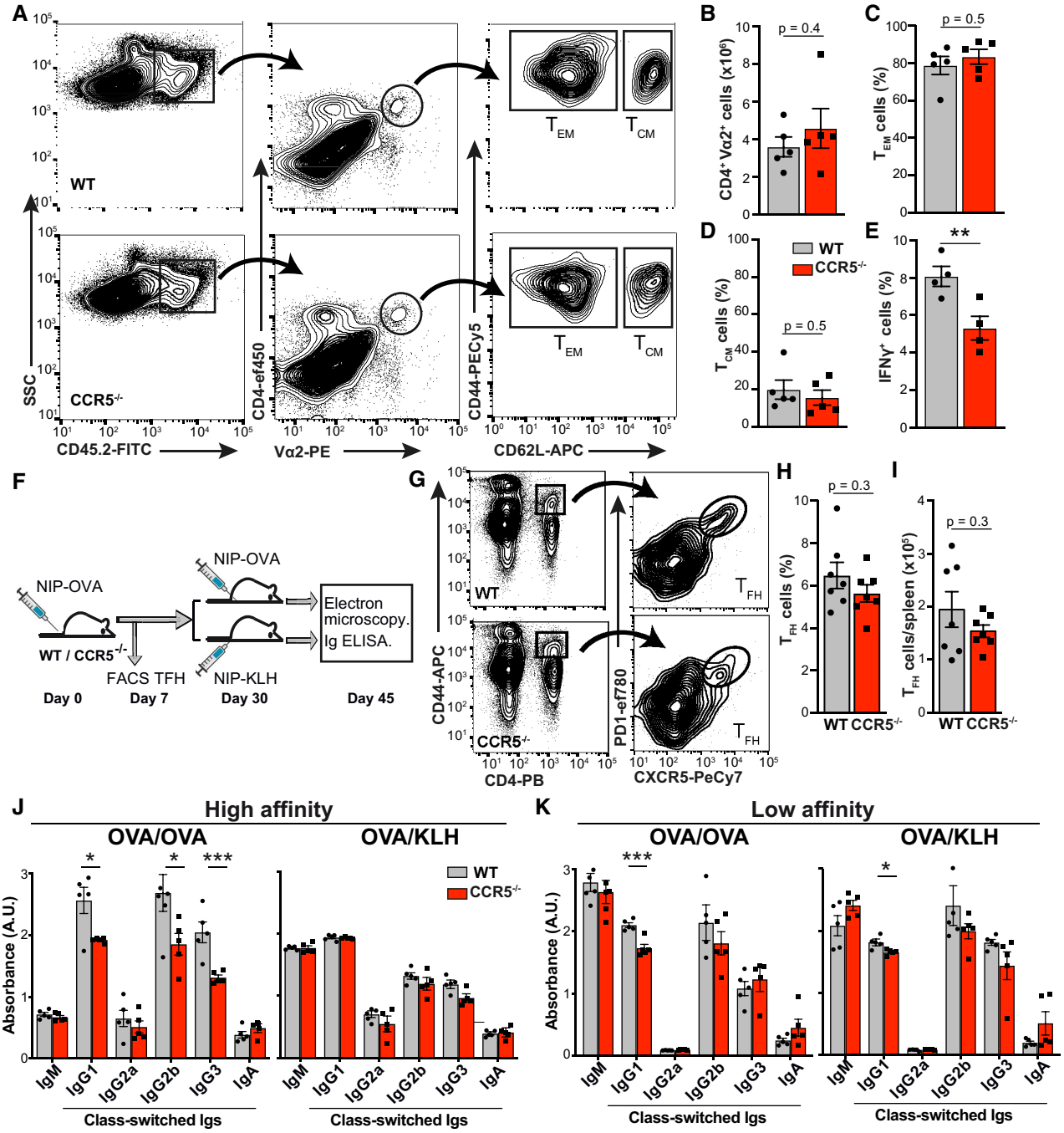

Figure 1. CCR5 deficiency impairs CD4⁺ T-cell memory responses.

A Representative plots of splenocytes from CD45.1 mice adoptively transferred with CD45.2 OT-II WT or CCR5$^{-/-}$ lymph node cell suspensions, 5 weeks after infection with rVACV-OVA virus. The gating strategy used to identify the memory CD4$^+$ T-cell subtypes is shown (n = 5).

B Absolute number of OT-II cells recovered in spleens of mice as in A (n = 5).

C, D Percentage of CD4$^+$ T_{EM} (C) and T_{CM} (D) in the OT-II WT and CCR5$^{-/-}$ populations (n = 5).

E IFNγ-producing OT-II WT and CCR5$^{-/-}$ memory cells isolated from mice as in (A) and restimulated *ex vivo* with $OVA_{323–339}$ (1 μM) (n = 4).

F Immunization scheme for NIP-OVA and NIP-KLH in WT and CCR5$^{-/-}$ mice.

G–I Representative plots (G) and quantification of the frequency (H) and absolute number (I) of T_{fh} cells (CD4$^+$CD44$^+$PD-1$^+$CXCR5$^+$) in the spleen after primary immunization (day 7) with NIP-OVA (n = 7).

J, K ELISA analysis of high- (J) and low-affinity (K) isotype-specific anti-NIP antibodies in sera from OVA/OVA- and OVA/KLH-immunized mice (day 15 post-challenge; n = 5 mice/group). Data representative of one experiment of two.

Data information: (B–E, H–K), Data are mean ± SEM. *P < 0.05, **P < 0.01, ***P < 0.001, two-tailed unpaired Student's t-test.

activation marker expression (CD25, CD69, CD44) compared to IL-2-cultured T cells (Fig 2A). Findings were similar in OT-II WT and CCR5$^{-/-}$ cells (Fig 2B), which reinforced the idea that CCR5 is not involved in CD4^{+} T memory cell differentiation. Restimulation of IL-2- or IL-15-expanded OT-II lymphoblasts with the OVA$_{323–339}$ peptide nonetheless indicated that CCR5-expressing cells showed strong proliferation and higher IL-2 production at low antigen concentrations than CCR5-deficient cells (Fig 2C–F), indicative of an increased number of cells responding to antigenic stimulation. CCR5 might thus increase the antigenic sensitivity of antigen-experienced CD4^{+} T cells in a cell-autonomous manner.

CCR5 modulates TCR nanoclustering in antigen-experienced CD4^{+} T cells

The high antigenic sensitivity of antigen-experienced CD8^{+} T cells was partially attributed to increased TCR nanoclustering (Kumar *et al*, 2011). To determine whether CCR5 deficiency influences TCR organization, we used electron microscopy (EM) to analyze surface replicas of OT-II WT and CCR5$^{-/-}$ naïve cells and lymphoblasts after labeling with anti-CD3ε antibody and 10 nm gold-conjugated protein A; a representative image of a IL-15-expanded WT lymphoblast is shown (Fig EV2). We found no differences in TCR

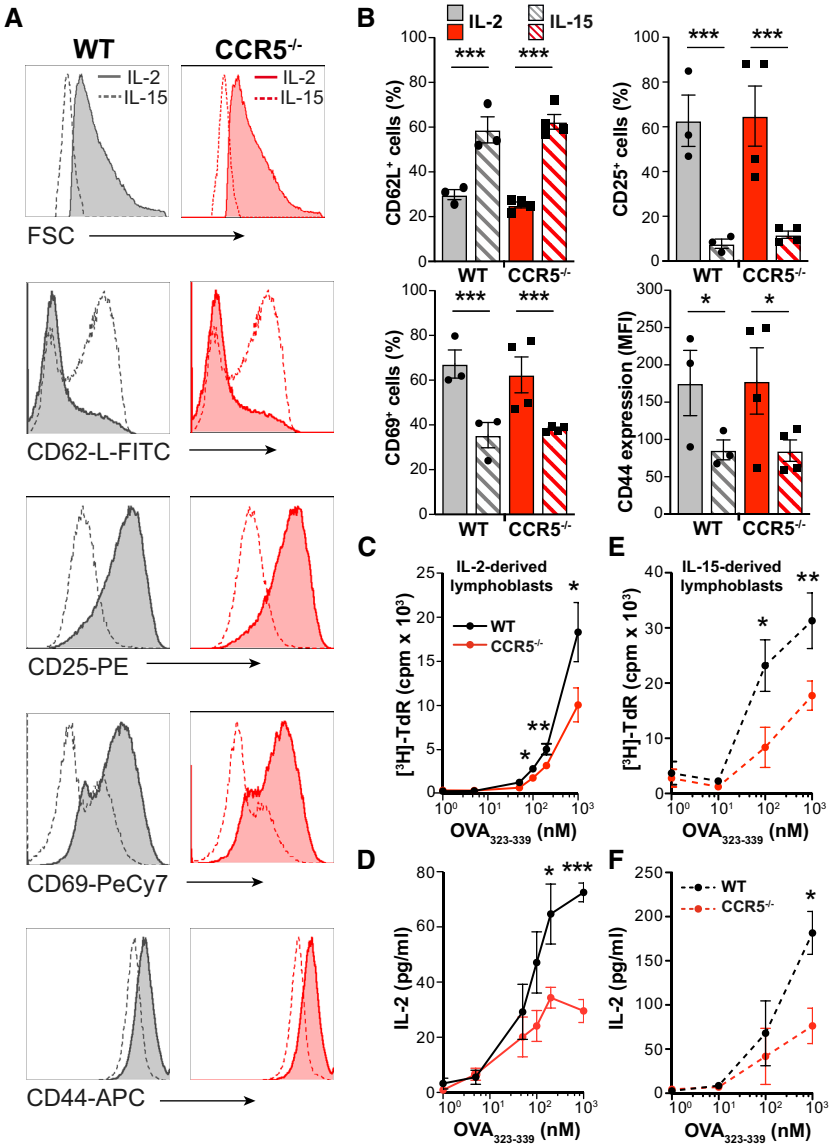

Figure 2. CCR5 increases the sensitivity of antigen-experienced CD4^{+} T cells.

A, B Representative histograms and quantification of mean fluorescence intensity (MFI; A) or the percentage of cells positive for the indicated memory markers (B) in OT-II WT and CCR5$^{-/-}$ lymphoblasts expanded in IL-2 or IL-15, as specified. Data shown as mean ± SEM ($n \geq 3$). The gating strategy is shown in Fig EV1.

C–F IL-2- (C, D) and IL-15-expanded lymphoblasts (E, F) were restimulated with indicated concentrations of OVA$_{323–339}$; cell proliferation (thymidine incorporation into DNA; C, E) and IL-2 production (by ELISA; D, F) were measured after 72 h. Data are presented as mean ± SEM (n = 5).

Data information: *P < 0.05, **P < 0.01, ***P < 0.001, two-way ANOVA (B) or two-tailed unpaired Student's t-test (C–F).

nanoclusters between OT-II WT and CCR5$^{-/-}$ naïve cells, which had a small percentage of TCR nanoclusters larger than 4 TCR in both genotypes (Fig 3A). In contrast, there was a significant increase in TCR nanocluster number and size in WT compared to CCR5$^{-/-}$ lymphoblasts (Fig 3B and C). The number of TCR nanoclusters per cell analyzed in each condition is also indicated (Appendix Table S1). As predicted, there was a gradient in TCR nanoclustering of naïve $\ll$ IL-2- < IL-15-differentiated OT-II WT cells (Appendix Fig S1E), which coincided with increased antigenic sensitivity of the IL-15-expanded cells (Appendix Fig S1F and G). These findings thus reinforce the IL-15-induced memory-like phenotype versus the IL-2-induced effector-like phenotype and link TCR nanoclustering with increased sensitivity in antigen-experienced CD4$^+$ T cells. The difference in TCR nanoclustering between WT and CCR5$^{-/-}$ cells was nevertheless similar in IL-2- and IL-15-expanded lymphoblasts, which indicates that CCR5 affects TCR nanoclustering in lymphoblasts independently of the cytokine milieu.

Using a Monte Carlo simulation, we applied data from surface replicas of naïve and IL-2-expanded OT-II lymphoblasts to determine whether the experimental frequency of cluster size was due to random distribution of gold particles. In all cases, the cluster distributions observed experimentally differed significantly from pure random proximity between clusters (Appendix Fig S2). To define the differences between OT-II WT and CCR5$^{-/-}$ cells, we used a model that accounts for receptor clustering dynamics (Castro *et al*, 2014), a Bayesian inference method that estimates the so-called clustering parameter, *b*. Based on this model, we concluded that the probability of a chance nanocluster distribution similar to that observed for naïve and activated OT-II WT and CCR5$^{-/-}$ cells approaches 0% (Fig 3D and E). Posterior distribution analysis also showed that whereas the clustering parameter was very similar between naïve OT-II WT and CCR5$^{-/-}$ cells (Fig 3D), there was clear separation in lymphoblasts (Fig 3E). These analyses provide a mathematical framework that validates the TCR nanoclustering differences between WT and CCR5$^{-/-}$ cells, as determined by EM.

The differences in TCR oligomerization between OT-II WT and CCR5$^{-/-}$ lymphoblasts were also studied using blue-native gel electrophoresis (BN-PAGE) (Schamel *et al*, 2005; Swamy & Schamel, 2009). Cell lysis with digitonin, a detergent that disrupts TCR nanoclusters into their monomeric components, showed that WT and CCR5$^{-/-}$ lymphoblasts expressed comparable TCR levels, as detected with anti-CD3ζ antibodies (Fig 3F). Cell lysis with Brij96, which preserves TCR nanoclusters, showed a notable reduction in large TCR complexes in CCR5$^{-/-}$ compared to WT lymphoblasts (Fig 3F). Two independent techniques thus support a CCR5 role in TCR nanoscopic organization in antigen-experienced CD4$^+$ T cells.

To determine whether CCR5 controls TCR nanoclustering in *in vivo*-generated memory T cells, we analyzed TCR distribution in surface replicas of CD4$^+$ memory T cells purified by negative selection from OVA/OVA-immunized WT and CCR5$^{-/-}$ mice (Appendix Fig S3). CD4$^+$ memory cells from CCR5$^{-/-}$ mice showed fewer, smaller TCR nanoclusters than those from WT counterparts (Fig 3G; Appendix Table S1), which indicates that CCR5 promotes formation of large TCR nanoclusters in endogenously generated CD4$^+$ memory T cells.

CCR5-induced TCR nanoclustering is independent of its co-stimulatory activity

Since CCR5 has co-stimulatory functions in CD4$^+$ T-cell priming (Molon *et al*, 2005; González-Martín *et al*, 2011), it is of interest to know whether defective TCR clustering in CCR5$^{-/-}$ lymphoblasts is due to suboptimal primary activation of these cells. To address this question, we treated OT-II WT cells with the CCR5 antagonist TAK-779 at various intervals throughout culture and analyzed TCR nanoclusters in IL-2-expanded T lymphoblasts. TAK-779 addition during the priming phase (blockade of CCR5 co-stimulatory function) decreased the percentage of large TCR nanoclusters compared to untreated controls (Fig 4A). TAK-779 treatment did not alter TCR clustering in OT-II CCR5$^{-/-}$ cells (Appendix Fig S4), which indicates that the TAK-779 effect on OT-II cells is CCR5-specific.

To avoid interference with the CCR5 co-stimulatory activity, we primed OT-II WT cells in the absence of the inhibitor and added TAK-779 only during IL-2-driven expansion of the CD4$^+$ lymphoblasts. In these conditions, TAK-779 also reduced the percentage of large TCR nanoclusters (Fig 4B), which indicates that the CCR5 signals that control TCR organization are independent of those involved in its co-stimulatory function.

We next explored whether other chemokine receptors involved in T-cell activation control TCR nanoclusters in CD4$^+$ T cells. CXCR4 is a paradigmatic chemokine receptor that also provides co-stimulatory signals (Kumar *et al*, 2006; Smith *et al*, 2013). We primed OT-II WT cells in the presence of the CXCR4 antagonist AMD3100 and analyzed TCR nanoclusters in IL-2-expanded T lymphoblasts. Vehicle- and AMD3100-treated cells showed similar TCR nanocluster distribution (Fig 4D), which implies that CXCR4 blockade does not interfere with TCR nanoclustering.

CCR5 deficiency increases ceramide levels in CD4$^+$ T cells

We analyzed CCR5 regulation of TCR nanoclustering in CD4$^+$ T cells and found no differences between OT-II WT and CCR5$^{-/-}$ cells in TCR/CD3 chain mRNA levels or in cell surface expression of the TCRα chain (Fig EV3). These data suggest that the reduction in TCR clustering in CCR5$^{-/-}$ cells is not due to decreased TCR expression.

T-cell antigen receptor nanoclustering is dependent on plasma membrane Chol and SM (Molnar *et al*, 2012), two lipids also necessary for CCR5 signaling (Mañes *et al*, 2001). OT-II WT and CCR5$^{-/-}$ lymphoblasts expressed comparable levels of total Chol and SM species (Fig 5A and B). OT-II CCR5$^{-/-}$ lymphoblasts nonetheless showed a significant increase in most ceramide (Cer) species and their dihydroCer (dhCer) precursors (Fig 5C and D). These differences were not observed in naïve OT-II WT and CCR5$^{-/-}$ cells (Appendix Fig S5A), indicative that the Cer increase was specific to antigen-experienced cells. The increase in Cer species in CCR5$^{-/-}$ lymphoblasts was not linked to enhanced apoptosis compared to WT cells (Appendix Fig S5B).

CCR5 deficiency upregulates specific ceramide synthases in CD4$^+$ T cells

Our analysis of the mRNA levels of key enzymes involved in Cer metabolism showed no differences in ceramidases (*ASAH1, ACER 2,*

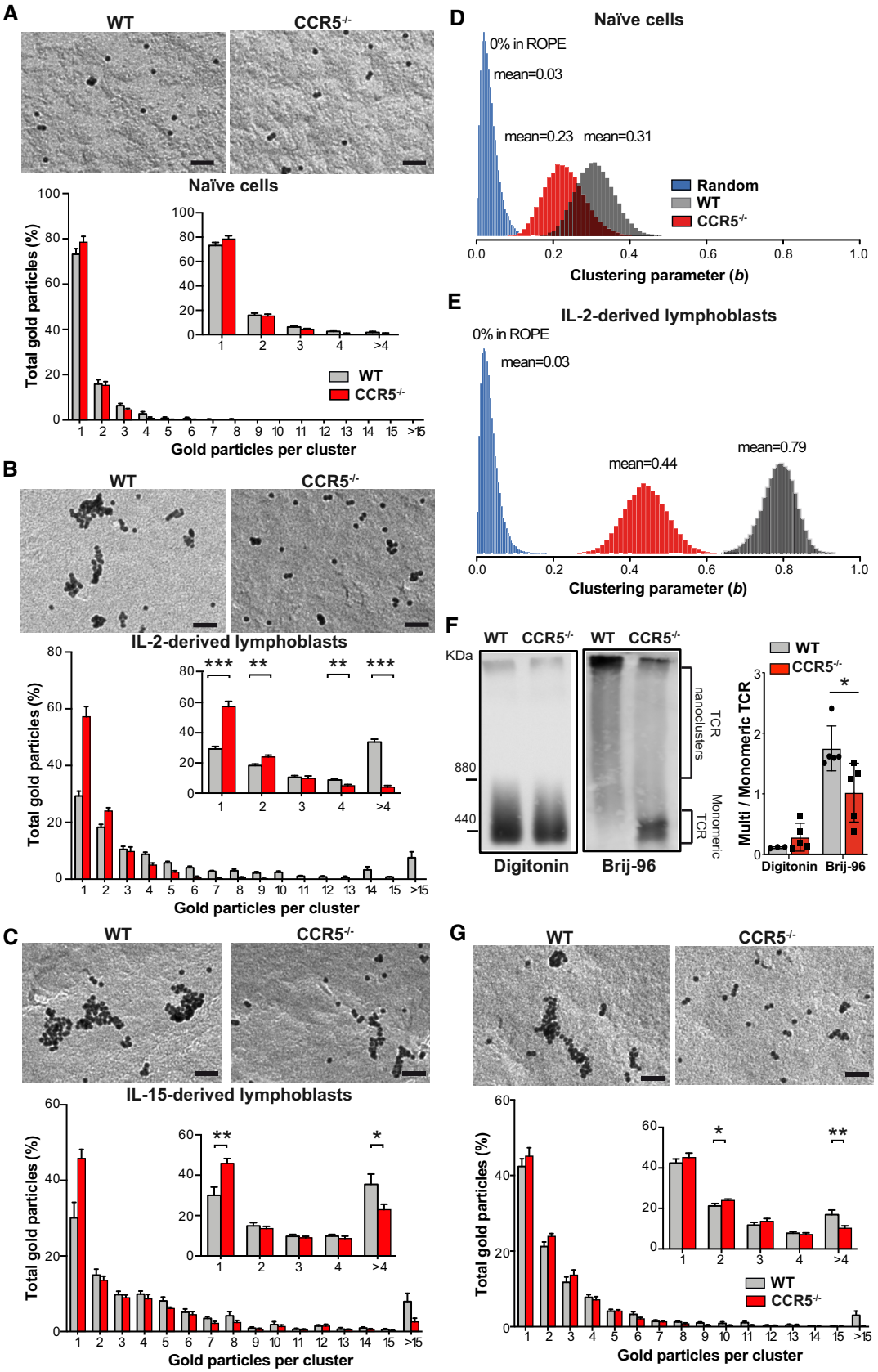

Figure 3.

Figure 3. CCR5 increases TCR nanoclustering in antigen-experienced CD4$^+$ T cells.

A–C Analysis of TCR nanoclustering by EM in OT-II WT and CCR5$^{-/-}$ naïve cells (A; n = 6 cells/genotype; WT: 3,427, CCR5$^{-/-}$: 3,528 particles), and IL-2- (B; WT, n = 8 cells, 15,419 particles; CCR5$^{-/-}$, n = 6 cells, 5,410 particles) or IL-15-expanded lymphoblasts (C; WT, n = 8 cells, 27,518 particles; CCR5$^{-/-}$, n = 7 cells, 22,696 particles). A representative small field image at the top of each panel shows gold particle distribution in the cell surface replicas of anti-CD3ε-labeled cells; at bottom, quantification (mean ± SEM) of gold particles in clusters of indicated size in WT (gray bars) and CCR5$^{-/-}$ cells (red). Insets show the distribution of clusters of one, two, three, four, or more than four particles, and statistical analysis.

D, E Posterior distribution in naïve (D) and IL-2-expanded lymphoblasts (E) of the clustering parameter b for WT (gray) and CCR5$^{-/-}$ cells (red); randomly generated distributions of receptors are shown in blue. The mean value of the b parameter is indicated for each condition. The probability of a chance distribution similar to that determined in cells is nearly 0% by the ROPE.

F Comparison of TCR oligomer size using BN-PAGE and anti-CD3ζ immunoblotting in day 10, IL-2-expanded WT and CCR5$^{-/-}$ OT-II lymphoblasts lysed in buffer containing digitonin or Brij-96. The marker protein is ferritin (f1, 440 and f2, 880 kDa forms). The ratio of TCR nanoclusters to monomeric TCR in each lysis condition was quantified by densitometry (right; n = 5).

G Top, representative small field EM images showing gold particle distribution in the cell surface replicas of CD4$^+$ T cells isolated from OVA/OVA-immunized WT and CCR5$^{-/-}$ mice. Bottom, quantification (mean ± SEM) of gold particles in clusters of the indicated size (WT, gray bars; n = 5 cells, 14,680 particles; CCR5$^{-/-}$, red; n = 7 cells, 15,374 particles). Insets show the distribution between clusters of one, two, three, four, or more than four particles, and statistical analysis.

Data information: (A–C, F, G), Data are mean ± SEM. *P < 0.05, **P < 0.01, ***P < 0.001, one-tailed unpaired Student's t-test. Scale bar, 50 nm (A–C, G).

ACER 3) and sphingomyelinases (*SMPD1–4*) between OT-II WT and CCR5$^{-/-}$ naïve cells or lymphoblasts (Fig EV4). mRNA levels of the ceramide synthases (CerS) CerS2, CerS3, and CerS4 were nonetheless upregulated in OT-II CCR5$^{-/-}$ lymphoblasts (Fig 5E); CerS5 and CerS6 were unaltered, and the nervous system-specific CerS1 isoenzyme was not detected. CerS2, CerS3, and CerS4 levels were comparable in naïve CD4$^+$ WT or CCR5$^{-/-}$ cells (Fig 5E), which again associate the CCR5 transcriptional effect on these genes with activation.

We sought to validate the CerS isoforms upregulated by CCR5 deficiency at the protein level. In accordance with mRNA analyses, CerS2 protein levels were significantly higher in CCR5$^{-/-}$ than in WT lymphoblasts (Fig 5F); CerS3 and CerS4 were undetectable or only barely detectable by immunoblot. This is consistent with the fact that CerS2 has the highest expression level and the broadest substrate specificity in other cell types (Laviad *et al*, 2008). Chromatin immunoprecipitation (ChIP), followed by amplification of a region of the CerS2 promoter enriched in CpG islands, showed that binding of the transcriptional activation marker acetylated histone H3K9 (H3K9Ac) was higher in CCR5$^{-/-}$ than in WT lymphoblasts (Fig 5G). Moreover, blockade of CCR5 signaling with pertussis toxin (PTx; an inhibitor of the $G\alpha_i$ subunit) also increased CerS2 mRNA expression (Fig 5H).

To further study CCR5 transcriptional regulation of CerS, we scanned for transcription factors with putative binding sites in the CerS2, CerS3, and CerS4 promoters, which are transcriptionally upregulated in CCR5$^{-/-}$ lymphoblasts, but not represented in the CerS6 promoter, which is not CCR5-regulated. We selected two regions; region 1 comprised −5 kb to the 5′UTR, and region 2 encompassed the 5′UTR to the first coding exon (Fig 5I). This bioinformatic approach identified GATA-1 and NF-IB (nuclear factor-1B) as putative transcription factors involved in the differential expression of the CerS2 isoform (Fig 5J and K).

We focused on GATA-1, since it is implicated in the differentiation of some CD4$^+$ T-cell subtypes (Sundrud *et al*, 2005; Fu *et al*, 2012). Immunofluorescence analyses showed increased nuclear levels of the phosphoSer142-GATA-1 form in OT-II CCR5$^{-/-}$ compared to WT lymphoblasts (Fig 5L and M), which correlated with enriched GATA-1 binding to the CerS2 promoter in CD4$^+$ CCR5$^{-/-}$ lymphoblasts (Fig 5N). CCR5 deficiency might induce CerS2 transcription through GATA-1.

Ceramide levels control TCR nanoclustering

We used a synthetic biology approach to determine whether ceramide content affects TCR nanoclustering. Large unilamellar vesicles (LUV) were prepared at different molar ratios of PC, Chol, SM, and Cer (Fig 6A) and then reconstituted with a streptavidin-binding-peptide-tagged TCR purified in its native state from murine M.mζ-SBP (streptavidin-binding peptide) T cells (Swamy & Schamel, 2009). The proteoliposomes were analyzed by BN-PAGE after solubilization in 0.5% Brij96 to maintain TCR nanocluster integrity or in 1% digitonin to disrupt TCR clusters. As anticipated (Molnar *et al*, 2012; Wang *et al*, 2016), TCR was monomeric in PC-containing LUV, whereas it formed nanoclusters when reconstituted in PC/Chol/SM liposomes (Fig 6B and C). The inclusion of ceramides in these LUV (PC/Chol/SM/Cer liposomes) reduced TCR nanoclustering in a dose-dependent manner. This effect was not due to differential TCR reconstitution in Cer-containing LUV, since digitonin treatment rendered equivalent levels of monomeric TCR in each condition (Fig 6B). These data suggest that Cer membrane content impairs TCR nanoclustering.

To test whether this effect also occurs in live cells, we treated OT-II WT lymphoblasts with recombinant sphingomyelinase (SMase), which hydrolyzes SM to ceramide (Kitatani *et al*, 2008). SMase treatment of WT OT-II blasts increased Cer levels robustly (Fig 6D), but did not compromise cell viability (Appendix Fig S6). Analysis of membrane replicas from these cells showed that SMase treatment reduced the number of high valency TCR nanoclusters compared to controls (Fig 6E; Appendix Table S1), which indicates that high Cer levels hinder TCR nanoclustering in CD4$^+$ T cells.

CerS2 silencing restores TCR nanoclustering after CCR5 functional blockade

To correlate increased CerS2 expression with the impaired TCR nanoclustering in OT-II CCR5$^{-/-}$ T cells, we attempted to silence CerS2 expression by lentiviral transduction of primary lymphoblasts with short-hairpin (sh) RNA for CerS2 or control (shCtrl). In the most successful experiments, we were only able to transduce ~ 20% of the lymphoblasts, which did not lead to solid CerS2 mRNA silencing (Appendix Fig S7A and B). Despite the low efficiency, antigenic restimulation tended to promote stronger responses in shCerS2-

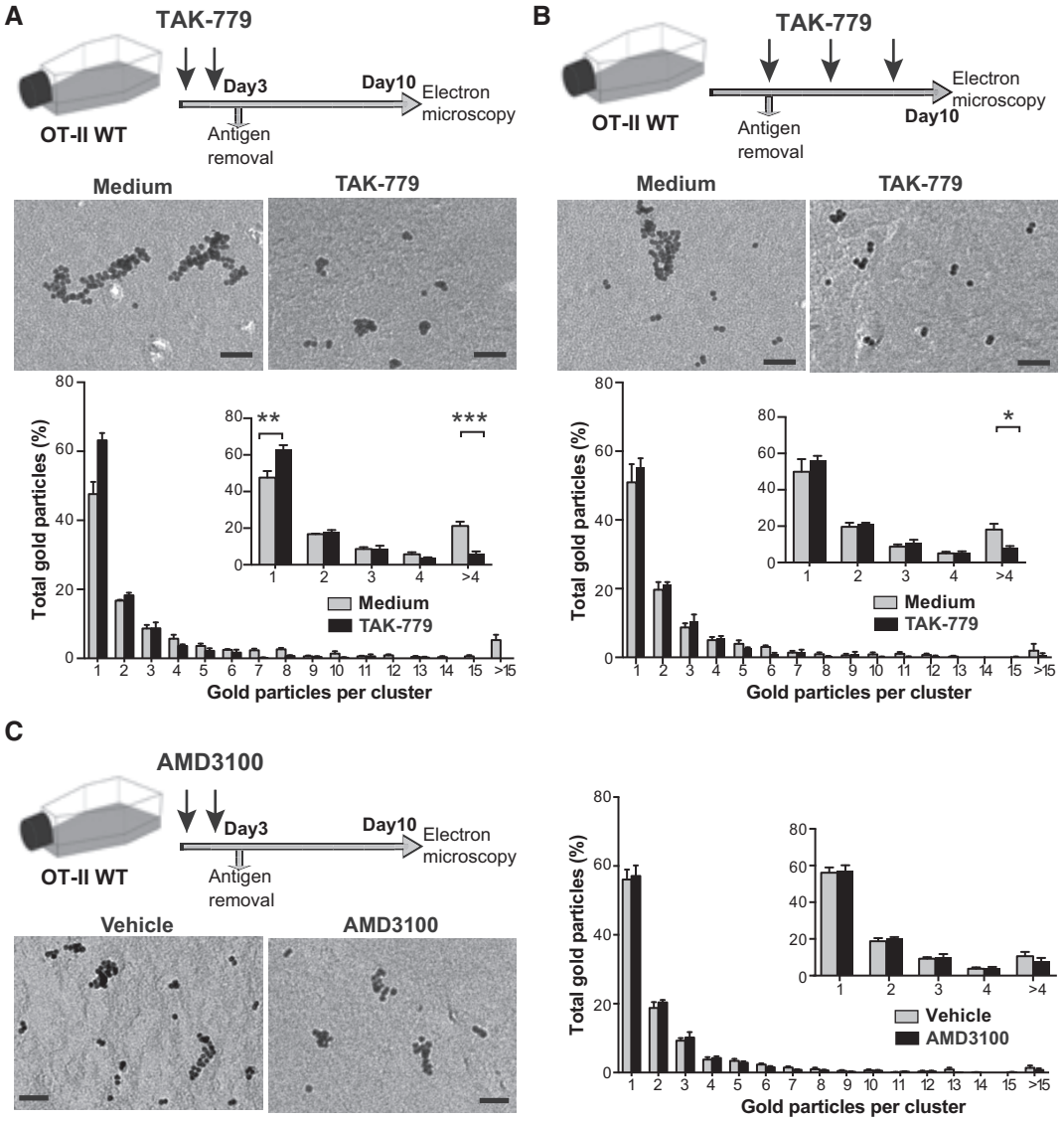

Figure 4. CCR5-induced TCR nanoclustering is specific and independent of its co-stimulatory activity.

A OT-II WT cells were activated with $OVA_{323–339}$, alone or with TAK-779. After 3 days, antigen and TAK-779 were removed and lymphoblasts expanded in IL-2-containing medium. TCR nanoclustering was analyzed in anti-CD3ε-labeled surface replicas of day 10 lymphoblasts. Top, representative small field EM images showing gold particle distribution in the cell surface replicas of WT $CD4^+$ T cells alone or with TAK-779. Bottom, quantification of gold particles in clusters of the indicated size. Inset, distribution of gold particles between clusters of one, two, three, four, or more than four particles in vehicle- (gray bars; n = 5 cells, 11,266 particles) and TAK-779-treated cells (black; n = 6 cells, 5,138 particles).

B OT-II WT cells were activated with $OVA_{323–339}$, and TAK-779 was added at days 3, 5, and 7 after antigen removal. Analysis as above, untreated (gray bars; n = 5 cells, 6,400 particles) and TAK-779-treated cells (black; n = 6 cells, 7,153 particles). Inset shows the distribution between clusters of one, two, three, four, or more than four particles, and statistical analysis.

C OT-II WT naïve cells were activated with antigen in the presence or not of the CXCR4 inhibitor AMD3100. Left, representative EM images showing gold particle distribution in the cell surface replicas. Right, analysis of gold particles in clusters as above, vehicle- (gray bars; n = 6 cells, 12,339 particles) and AMD3100-treated cells (black; n = 7 cells, 17,059 particles). Inset shows the distribution between clusters of one, two, three, four, or more than four particles, and statistical analysis.

Data information: (A–C), Data are mean ± SEM. $*P < 0.05$, $**P < 0.01$, $***P < 0.001$, one-tailed unpaired Student's t-test. Scale bar, 50 nm.

than in shCtrl-transduced cells (Appendix Fig S7C and D). The low efficiency also precluded analysis of TCR nanoclusters in membrane replicas, as transduced cells could not be distinguished from non-transduced cells.

To overcome these difficulties, we used the 2B4 $CD4^+$ T-cell line. We verified that 2B4 cells expressed CCR5 and that TAK-779 treatment increased CerS2 levels and impaired TCR nanoclustering (Appendix Fig S8). The data suggest that CCR5 effects on TCR nanoclustering and CerS2 induction are not exclusive to the OT-II system and that TAK-779-treated 2B4 cells mimic the functional findings in OT-II $CCR5^{-/-}$ lymphoblasts. 2B4 cells were transduced efficiently by lentiviruses and, after

3 days of antibiotic selection, 100% of the cells expressed the shRNA; this led to strong silencing of CerS2 mRNA and protein in shCerS2- compared to shCtrl-transduced cells (Fig 6F–H). Analysis of TCR organization showed recovery of large TCR nanoclustering in TAK-779-treated, shCerS2-transduced cells compared to controls (Fig 6I; Appendix Table S1); after restimulation with plate-bound anti-CD3ε antibody in the presence of TAK-779, CD69 upregulation was higher in CerS2-deficient than in shCtrl-cells (Fig 6J).

CCR5 modulates TCR nanoclustering in human CD4$^+$ T cells

Finally, we tested whether CCR5 deficiency also impairs TCR organization in human CD4$^+$ T cells. Approximately 1% of the

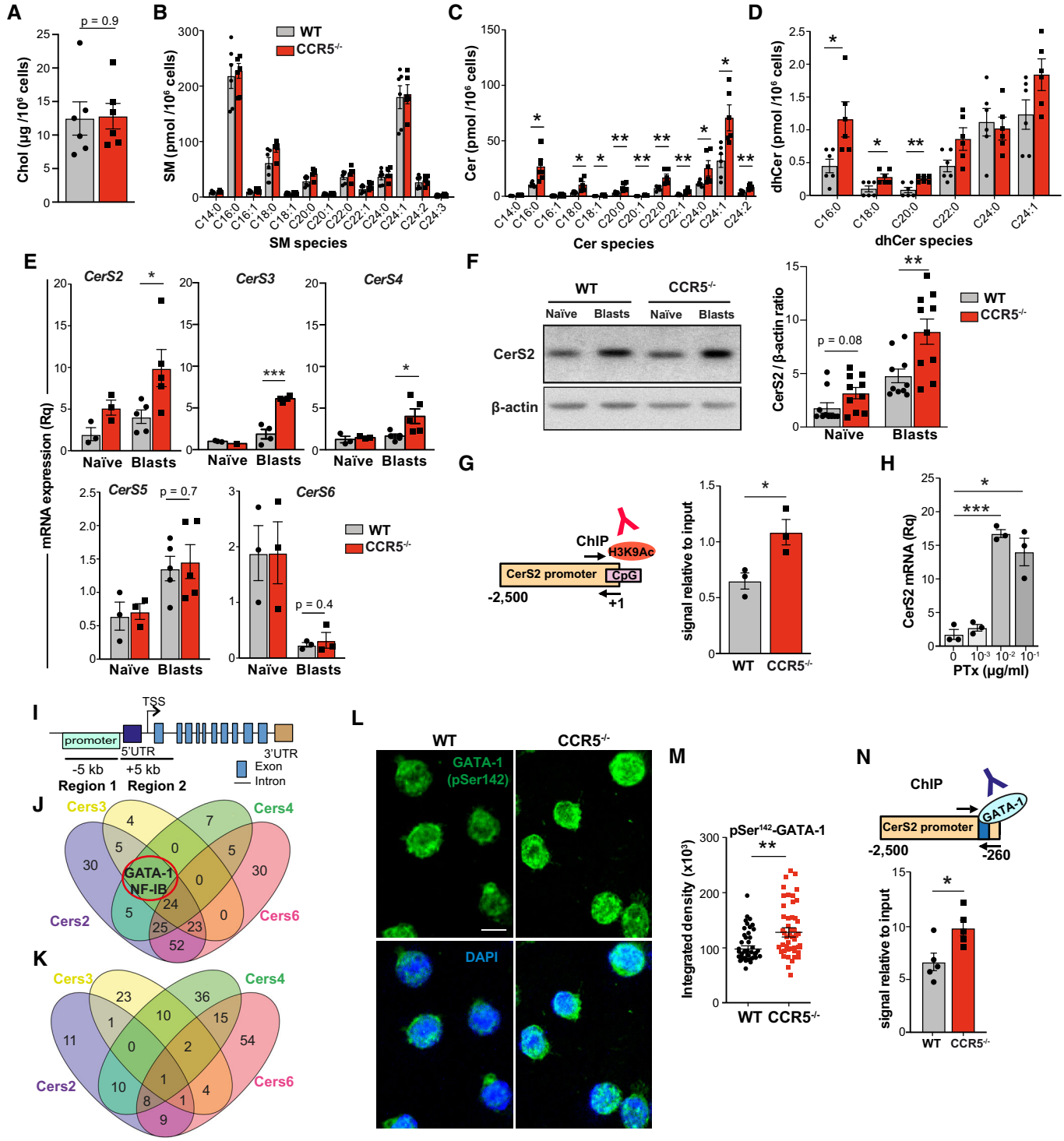

Figure 5.

Figure 5. CCR5 deficiency increases Cer levels by upregulating specific CerS.

A Total Chol levels in WT and CCR5$^{-/-}$ OT-II lymphoblasts (day 10, IL-2-expanded) as determined by a fluorometric assay (n = 6).

B–D SM (B), Cer (C) and dhCer (D) levels in WT and CCR5$^{-/-}$ OT-II 10-day lymphoblasts, as determined by UPLC-TOF MS. Values, after normalization with C17 standards and cell number in each sample, are the mean of two independent experiments (n = 6).

E RT–qPCR determination of CerS mRNA levels in naïve and IL-2-expanded WT and CCR5$^{-/-}$ OT-II 10-day lymphoblasts (n = 3–5).

F Representative immunoblot showing CerS2 protein levels in naïve and WT and CCR5$^{-/-}$ OT-II 10-day lymphoblasts, and densitometric quantification of blots as above (n = 10).

G ChIP analysis of the CerS2 promoter using an anti-H3K9Ac antibody. Scheme of the CerS2 promoter showing CpG islands and primers used for amplification. Relative ChIP of the CerS2 promoter in WT and CCR5$^{-/-}$ OT-II 10-day lymphoblasts (n = 3).

H Relative CerS2 mRNA level in CD4 T cells treated with PTx (n = 3).

I Scheme of a canonical CerS gene to illustrate the *in silico* strategy used to search for CerS-specific transcription factors.

J, K Venn diagrams showing the number of transcription factors with putative binding sites in the indicated CerS genes in regions 1 (J) and 2 (K). The red circle highlights the transcription factors shared by CerS2, CerS3, and CerS4 promoters, but not present in the CerS6 promoter.

L Representative immunofluorescence images showing pSer142-GATA-1 staining (green) of OT-II WT and CCR5$^{-/-}$ lymphoblasts. The green channel (top) and the merge with nuclear DAPI staining (blue; bottom) are shown. Scale bar, 10 μm.

M Quantification of nuclear staining of the cells plotted as integrated density fluorescence intensity in DAPI-stained area ($n \geq 50$ cells/condition).

N Top, basic scheme of the CerS2 promoter, indicating the putative GATA-1 binding site (blue) and location of the primers used for amplification in ChIP assays (black arrows). Bottom, relative anti-GATA-1 ChIP levels in OT-II WT and CCR5$^{-/-}$ lymphoblasts (n = 5).

Data information: (E, G, H, N), Each data point is the average of triplicates in an independent experiment. (A–H, M, N), Data shown as mean ± SEM of triplicates; *$P < 0.05$, **$P < 0.01$, ***$P < 0.001$, two-tailed unpaired Student's t-test.
Source data are available online for this figure.

Spanish population bears the *ccr5*Δ32 polymorphism in homozygosity (Mañes *et al*, 2003). Purified CD4$^+$ T cells from healthy WT or *ccr5*Δ32 homozygous donors were activated with anti-CD3 and anti-CD28 antibodies for 3 days and maintained for five additional days with IL-2. We found that *ccr5*Δ32 lymphoblasts had a lower percentage of large TCR nanoclusters than WT cells (Fig 7A; Appendix Table S1); concomitantly, the fraction of monomeric TCR was increased in the former. Sphingolipid analysis of these CD4$^+$ lymphoblasts showed an increase in saturated 24-carbon Cer (C24:0) and its precursor (dhCer C24:0) in cells derived from *ccr5*Δ32 donors, whereas SM levels were comparable between both genotypes (Fig 7B). This increase in Cer levels was associated with upregulation of CerS2 mRNA in *ccr5*Δ32 lymphoblasts compared to WT controls (Fig 7C); expression of other enzymes involved in Cer metabolism was unchanged in both genotypes (Fig EV5). These results indicate that, as found in mouse CCR5$^{-/-}$ lymphoblasts, antigen-experienced human CD4$^+$ T cells from *ccr5*Δ32 homozygotes show defective TCR nanoclustering associated with increased Cer levels and upregulated CerS2. Moreover, they indicate that these CCR5 effects are not restricted to specific T-cell clones, but can be observed in a polyclonal T-cell repertoire.

Discussion

Here, we show that CCR5 signaling is largely dispensable for memory CD4$^+$ T-cell differentiation, but provides specific signals that improve the functional fitness of memory cells after antigen reencounter. The CCR5 signals optimize TCR nanoclustering and antigen sensitivity by triggering a CD4$^+$ T-cell-specific transcription program that regulates Cer metabolism. This CCR5 program operates in murine and human CD4$^+$ T cells, which suggests physiopathological relevance.

A central observation of our study is that CCR5 expression enhances the degree of TCR nanoclustering in resting antigen-experienced T cells, both *in vitro* and *in vivo*. The presence of TCR nanoclusters in resting T cells was shown by BN-PAGE, EM, and super-resolution microscopy (Schamel *et al*, 2005; Hu *et al*, 2016; Jung *et al*, 2016; Pageon *et al*, 2016). We demonstrate here differential TCR nanoclustering in WT and CCR5-deficient cells using two complementary approaches (EM and BN-PAGE), based on different conceptual principles. In EM, TCR nanoclusters were defined as gold particle aggregates at < 10 nm distance from one another. Previous analyses showed that this criterion permits identification of TCR nanoclusters formed by TCR-TCR interactions (Kumar *et al*, 2011); these tightly associated TCR nanoclusters would allow inter-TCR cooperativity for pMHC binding (Martín-Blanco *et al*, 2018). We therefore intentionally considered TCR not to be in the same nanocluster if the gap between them was > 10 nm; this excludes considering more loosely associated TCR as nanoclusters, but the strict definition allowed association of TCR nanoclusters to a T-cell biological function.

It is also important to clarify that gold particle counts do not necessarily correspond to the number of TCR molecules in a nanocluster. BN-PAGE defines neither the exact size nor the abundance of TCR nanoclusters. Direct comparison of CCR5$^{-/-}$ with WT cells using both methods nonetheless allowed us to detect relative differences and determine the promoter effect of CCR5 in TCR nanoclustering. Application of Monte Carlo simulations further indicated that the nanoclusters observed in EM are not the result of random proximity of gold particles. The estimated clustering parameter (b) for randomly distributed particles was virtually zero.

Since CCR5 provides positive signals during activation of naïve CD4$^+$ T cells (Molon *et al*, 2005; Nesbeth *et al*, 2010; González-Martín *et al*, 2011), we attempted to clarify whether TCR nanoclustering impairment in CCR5$^{-/-}$ cells is solely an effect of this defective priming. This is unlikely, since TCR clustering was inhibited when CCR5 was blocked during expansion of fully activated WT lymphoblasts. This effect on TCR nanoclustering during lymphoblast expansion was modest compared to that observed in the priming phase, but is probably the result of insufficient CCR5 inhibition during lymphoblast expansion. CCR5 is not only upregulated shortly after activation, but is maintained in memory CD4$^+$ T cells, which are highly susceptible to

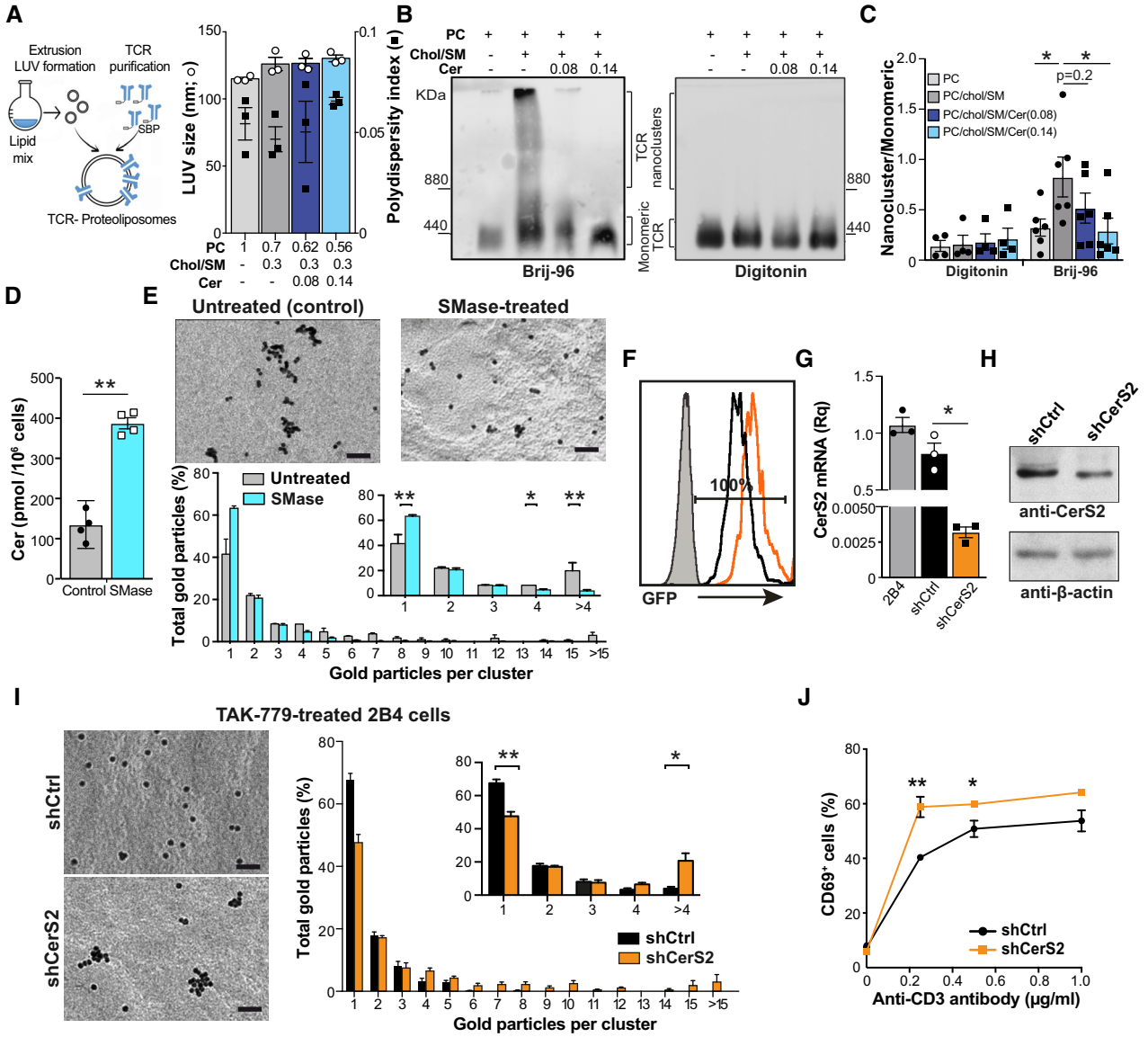

Figure 6. Cer levels determine the grade of TCR nanoclustering.

A Scheme of the strategy used to form TCR proteoliposomes, and size of LUV generated at the indicated lipid molar ratio. Polydispersity index values are shown as black squares for each condition (n = 3). SBP, streptavidin-binding-peptide-tagged TCR.

B Representative immunoblots comparing TCR nanocluster sizes via BN-PAGE and anti-CD3ζ immunoblotting in TCR proteoliposomes lysed in the presence of Brij-96 or digitonin. The marker protein is ferritin (f1, 440 and f2, 880 kDa forms).

C The ratio of the nanocluster and monomeric TCR in each lysis condition was quantified by densitometry from immunoblots as in (B) ($n \geq 4$).

D Cer levels in OT-II 10-day lymphoblasts, untreated or treated with SMase (n = 4).

E Representative small field images showing gold particle distribution, and quantification (mean ± SEM) of gold particles in clusters of the indicated size in cell surface replicas from untreated (gray bars; n = 5 cells, 8,126 particles) and SMase-treated (1 h) OT-II lymphoblasts (cyan; n = 6 cells, 8,457 particles) after CD3ε labeling, as determined by EM. The inset shows distribution between clusters of one, two, three, four, or more than four particles.

F GFP expression in shCtrl- (black) and shCerS2 (orange)-transduced 2B4 cells after puromycin selection, as determined by FACS. Non-transfected 2B4 cells (gray).

G Relative CerS2 mRNA levels in TAK-779-treated 2B4 cells as in (F). Values were normalized to those obtained in untransduced TAK-779-treated 2B4 cells (n = 3).

H Representative immunoblot with anti-CerS2 antibody to determine CerS2 protein levels in shCtrl and ShCerS2-transduced 2B4 cells as in (G). Filters were rehybridized with β-actin as loading control.

I TCR nanoclustering of shCtrl- and shCerS2-transduced 2B4 cells in the presence of TAK-779 as determined by EM. Representative small field images and quantification (mean ± SEM) of gold particles in clusters of indicated sizes in cell surface replicas shCtrl (black bars; n = 6 cells, 12,337 particles) and shCerS2 2B4 lymphoblasts (orange; n = 7 cells, 13,456 particles). Inset, distribution between clusters of indicated size and statistical analysis.

J Percentage of CD69$^+$ shCtrl (black) and shCerS2 (orange) 2B4 cells restimulated with plate-bound anti-CD3ε antibody in the presence of TAK-779 (n = 3).

Data information: (A, C–E, G–J), Data are shown as mean ± SEM. *P < 0.05, **P < 0.01, one-tailed (E, I) or two-tailed unpaired Student's t-test. Scale bar, 50 nm.
Source data are available online for this figure.

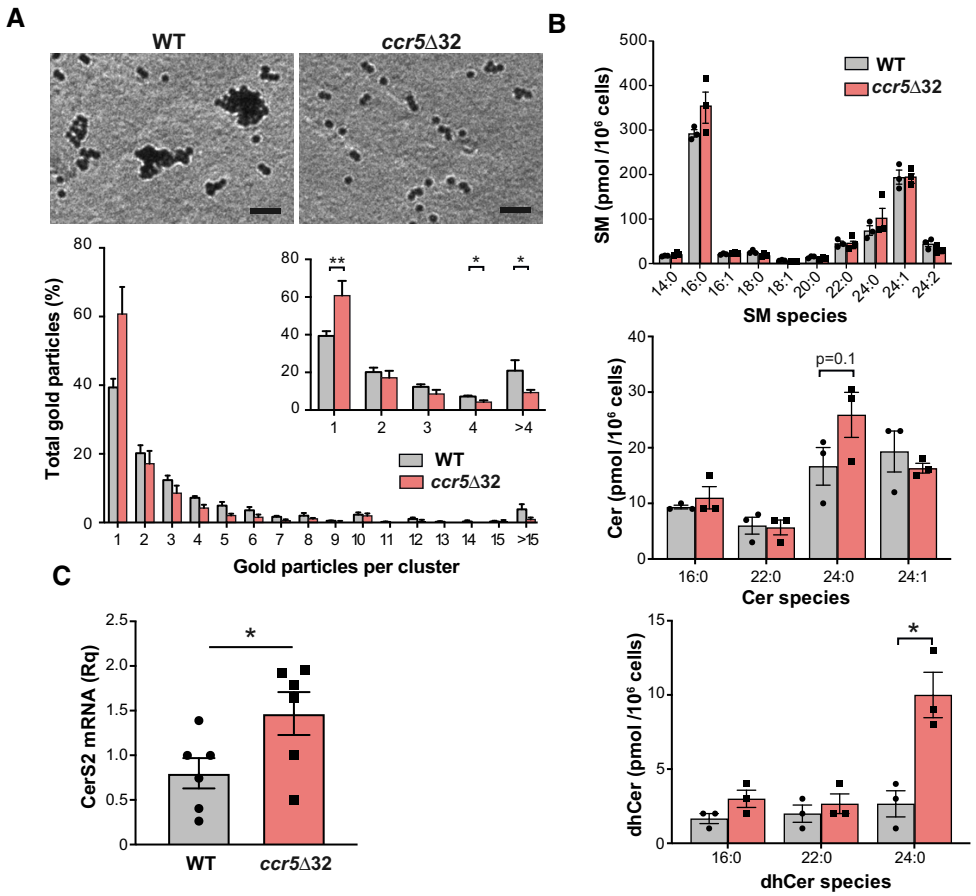

Figure 7. CCR5 controls TCR nanoclustering and Cer metabolism in human CD4$^+$ cells.

A Analysis of TCR nanoclustering in lymphoblasts from healthy WT and *ccr5*Δ32 homozygous donors by EM. Top, representative small field image showing gold particle distribution in cell surface replicas of anti-CD3ε-labeled cells; bottom, quantification (mean ± SEM) of gold particles in clusters of the indicated size in the WT (gray bars; n = 5 cells, 17,689 particles) and Δ32/Δ32 cells (light red; n = 4 cells, 16,938 particles). Insets show the distribution between clusters of one, two, three, four, or more than four particles, and statistical analysis.

B Normalized SM, Cer, and dhCer levels in lymphoblasts obtained as in (A). A representative experiment is shown (n = 3 donors/genotype; n = 2 independent experiments).

C Relative CerS2 mRNA levels in day 8 WT and *ccr5*Δ32 lymphoblasts. Each data point is the average of a technical triplicate from three donors in two independent experiments (n = 6).

Data information: Data are shown as mean ± SEM (B, C). *P < 0.05, **P < 0.01, two-tailed unpaired Student's t-test. Scale bar, 50 nm.

infection by R5-tropic HIV-1 strains (Nie *et al*, 2009). Our results showed increased CCR5 mRNA expression during lymphoblast expansion. These lymphoblasts also expressed CCR5 ligands, suggesting autocrine CCR5 stimulation during this phase. We thus propose that TCR nanoclustering is regulated by CCR5 signals transduced during lymphoblast differentiation rather than during priming.

Another feature that distinguishes CCR5 effects on priming and on TCR nanoclustering is the role of CXCR4 in these events. During priming, CCR5 and CXCR4 are recruited to and accumulate as heteromeric complexes at the IS of CD4$^+$ T cells; AMD3100 (a CXCR4 antagonist) prevented not only CXCR4 but also CCR5 accumulation (Contento *et al*, 2008), which indicates necessary cooperation between CCR5 and CXCR4 for full T-cell activation. In contrast, AMD3100 did not affect TCR nanoclusters in CCR5-expessing cells, which suggests that CXCR4/CCR5 heterodimer signaling is not essential for TCR nanoclustering in lymphoblasts. CCR5 homo- and heterodimers are thought to associate differently with Gα subunits; homodimers signal through the PTx-sensitive $G\alpha_i$, whereas heterodimers generate PTx-resistant responses (Mellado *et al*, 2001). CCR5 co-stimulatory signals in the IS are PTx-resistant (Molon *et al*, 2005), consistent with CCR5/CXCR4 heterodimerization during priming. PTx potentiates transactivation of the CerS2 promoter (Fig 5H), however, which suggests involvement of the CCR5-induced $G\alpha_i$ pathway in TCR nanoclustering. CCR5 thus appears to trigger distinct signaling pathways for co-stimulation and TCR nanoclustering in CD4$^+$ T cells. Since chemokine receptors can form nanoclusters (Martinez-Muñoz *et al*, 2018), it would be of interest to study potential feedback loops between TCR and CCR5 nanoclusters.

Cholesterol and SM are two lipids essential for CCR5 signaling and TCR nanoclustering (Mañes *et al*, 2001; Molnar *et al*, 2012). In

resting T cells, these receptors nonetheless partition in different membrane phases, liquid-ordered (l_o) for CCR5 (Molon *et al*, 2005) and liquid-disordered (l_d) for TCR (Beck-Garcia *et al*, 2015). This differential phase segregation argues against direct CCR5/TCR interaction as a mechanism that influences TCR nanoclustering. Our results suggest instead that increased levels of long-chain Cer species cause defective TCR nanoclustering in CCR5$^{-/-}$ lymphoblasts. Indeed, elevation of Cer levels in TCR-reconstituted proteoliposomes and in live cells by SM hydrolysis impaired nanoscopic TCR organization. Although Cer levels were higher in lymphoblasts than in naïve cells, which supports a role for Cer in T-cell activation (Sofi *et al*, 2017), CCR5 deficiency further increased Cer levels specifically in lymphoblasts. The Cer increase in CCR5$^{-/-}$ lymphoblasts did not cause spontaneous apoptosis (Appendix Fig S6B), which coincides with the non-apoptotic and preventive effects of long-chain Cer in this process (Stiban & Perera, 2015).

Although Cer levels increased in antigen-experienced CD4$^+$ T cells from CCR5$^{-/-}$ mice and ccr5Δ32 homozygotes, there were differences between the mouse and the human cell ceramidome. This could depend on many factors, including the overall species-specific enzymes involved in sphingolipid metabolism, or the lipid composition of the diet. Membrane phase segregation properties of ceramides are dependent not only on the saturation, but also on the length of their acyl chain and the lipid microenvironment that surrounds them (Alonso & Goñi, 2018). Although C24:1 is the most abundant Cer in mouse WT and CCR5$^{-/-}$ T cells, the biggest differences associated with CCR5 deficiency were observed for C20:0 and C22:0 Cer. The differential membrane phase segregation properties of C24:0 and C24:1 Cer might be subtle in an environment enriched in other long-chain saturated Cer and dhCer.

Several settings can be hypothesized that explain Cer effects on TCR nanoclustering. In model membranes, Cer has strong segregation capacity, which might affect their lateral organization (Alonso & Goñi, 2018). When the Chol concentration is saturating, however, as is the case of cell membranes and our proteoliposomes, Cer-enriched domains are not formed, due to the ability of Chol and Cer to displace one another (Castro *et al*, 2009). This argues against the idea that Cer impairs TCR clustering by promoting a general reduction in membrane lateral diffusion. Our mathematical model also predicted that cluster distribution is independent of TCR diffusivity. Interaction of the TCRβ subunit with Chol/SM complexes is critical for TCR nanoclustering (Molnar *et al*, 2012; Wang *et al*, 2016). High levels of Cer or their precursors (dhCer) could transform Chol/SM into Chol/SM/Cer domains with specific physicochemical properties, which might hinder TCR nanocluster formation physically or thermodynamically. For instance, high dhSM levels inhibit CCR5-mediated HIV-1 infection by rigidifying CCR5-containing l_o domains (Vieira *et al*, 2010). Chol/SM interaction depends on the hydrogen bond generated by the amide group of the SM molecule and the 3-hydroxyl group of Chol (Ramstedt & Slotte, 2002), but the SM amide group can also form hydrogen bonds with the Cer hydroxyl group (Garcia-Arribas *et al*, 2016). It is thus possible that, rather than forming SM/Chol/Cer domains, small increases in Cer levels would increase the mutual displacement of three lipids. This could lead to replacement of SM/Chol by SM/Cer complexes with gel-like biophysical properties (Sot *et al*, 2008).

Our results indicate that the CCR5 effect on TCR clustering is biologically meaningful. In a first model, we show that the responses of CCR5-deficient memory CD4$^+$ T cells generated by vaccination were impaired after *ex vivo* stimulation. In a second model that involves T:B-cell cooperation, we show that CCR5 deficiency impaired class switching of high-affinity antibodies after re-exposure to a T cell-dependent antigen. Affinity maturation and class switching depend on recruitment of T_{fh} cells to GC (Vinuesa *et al*, 2016). This T_{fh} cell confinement is a result of CXCR5 expression and the downregulation of other homing receptors, including CCR5 (Crotty, 2011), which could explain the lack of difference in class switching between OVA/KLH-immunized WT and CCR5$^{-/-}$ mice. There were also no differences between WT and CCR5$^{-/-}$ effector T_{fh} cells after the first OVA immunization. Once GC resolve, however, some T_{fh} cells are reported to enter the circulation as T_{fh} central memory-like cells (Vinuesa *et al*, 2016). These circulating, antigen-experienced T_{fh} cells express CCR5 and are very susceptible to HIV-1 infection (Xu *et al*, 2017). We found that the frequency of large TCR nanoclusters increased in memory T cells from WT compared to CCR5$^{-/-}$ OVA/OVA-immunized mice, which suggests increased antigenic sensitivity.

We hypothesize that following re-exposure to antigen, CCR5-expressing memory pre-T_{fh} cells will have a more efficient response than CCR5-deficient cells, which would support robust antibody responses after their differentiation to GC-T_{fh} cells. In humans, functional CCR5 deficiency does not cause strong immune suppression, but *ccr5*Δ32 homozygosity was associated with four times more fatal infections than average during the 2009–2011 influenza season in Spain (Falcon *et al*, 2015) and fatal infections by the West Nile Virus in the United States (Lim & Murphy, 2011). Our results provide a conceptual framework on which to base clinical trials to evaluate CD4$^+$ T-cell memory responses in CCR5-deficient humans, and suggest caution regarding the risks associated with genetic ablation of CCR5 as a preventive strategy to block HIV-1 infection.

Material and Methods

Resource Identification Portal accession numbers for antibodies, cell lines, animals, and other reagents used in the study are provided in Appendix Table S2.

Antibodies and reagents

Antibodies used to characterize mouse cells by flow cytometry were anti-Vα_2TCR-PE (B20.1), anti-CD25-PE (PC61), anti-CD45.2-FITC (104), anti-CD62L-FITC/APC (MEL-14), anti-CD69-PeCy7 (H1.2F3), and biotinylated anti-CXCR5 (2G8) from BD Biosciences; anti-human biotinylated CD3 (OKT3), anti-CD4-PeCy7/eFluor450/Pacific Blue (RM4.5), anti-IFNγ-APC (XMG1.2), and anti-PD1-eFluor780 (J43) from eBioscience; and anti-CD44-PeCy5/APC (IM7) from BioLegend. Biotinylated and purified anti-CD3ε (145-2C11; BD Biosciences) were used for EM and T-cell activation, respectively. Anti-mouse CerS-2 (1A6; Novus Biologicals), anti-CD3ζ (449, purified from hybridoma), and anti-β-actin (AC-15; Sigma-Aldrich) were used for immunoblot. Anti-mouse GATA-1 (D52H6; Cell Signaling) and anti-mouse phospho-GATA1^{pSer142} (Thermo Fisher Scientific) were used for immunofluorescence. Anti-GATA1 (ab11852, Abcam), anti-histone H3Lys9 (CS200583), and purified IgG rabbit (PP64B; EMD Millipore) were used for ChIP.

The $OVA_{323–339}$ peptide was synthesized at the CNB Proteomics facility. TAK-779, AMD-3100, poly-L-lysine, pertussis toxin, Cer (bovine spinal cord), and sphingomyelinase (*Bacillus cereus*) were from Sigma-Aldrich. mCCL4, mIL-2, and mIL-15 were from PeproTech; NIP-KLH, NIP-OVA, NIP(7)-BSA, and NIP(41)-BSA were from Biosearch Technology. Soybean phosphatidylcholine Chol, egg SM, C12 Cer (d18:1/12:0), C16 Cer (d18:1/16:0), C18 Cer (d18:1/18:0), C24 Cer (d18:1/24:0), C24:1 Cer (d18:1/24:1(15Z)), C16 dhCer (d18:0/16:0), C18 dhCer (d18:0/18:0), C24 dhCer (d18:0/24:0), C24:1 dhCer (d18:0/24:1(15Z)), C12:0 SM (d18:1/12:0), C16:0 SM (d18:1/16:0), C18:0 SM (d18:1/18:0), C24:0 SM, C24:1 SM, and the Cer mix from bovine spinal cord were from Avanti Polar Lipids. Lentiviral pGIPZ containing shRNAs for murine Cers 2 (V3LMM_454307, V3LMM_454309, and V3LMM_454311 clones), and the mismatched control were from Dharmacon.

Mice and cell lines

C57BL/6J WT and $CCR5^{-/-}$ mice were from The Jackson Laboratory. TCR transgenic OT-II $CCR5^{-/-}$ mice, recognizing $OVA_{323–339}$ (ISQAVHAAHAEINEAGR; I-Ab MHC class II molecule), have been described (González-Martín *et al*, 2011). B6-SJL (Ptprca Pepcb/BoyJ) mice bearing the pan-leukocyte marker allele CD45.1 were used for adoptive transfer experiments. CD3ε-deficient mice (DeJarnette *et al*, 1998) were used as a source of antigen-presenting cells for restimulation assays. Mice were maintained in SPF conditions in the CNB and CBM animal facilities, in accordance with national and EU guidelines. All animal procedures were approved by the CNB and the Comunidad de Madrid ethical committees (PROEX 277/14; PROEX 090/19). Human embryonic kidney HEK-293T cells and the murine 2B4 hybridoma and its derivative M.mζ-SBP (which expresses a SBP-tagged form of CD3ζ) (Swamy & Schamel, 2009) were cultured in standard conditions.

Isolation and culture of mouse and human primary T cells

Spleen and lymph nodes from 6- to 12-week-old OT-II WT and $CCR5^{-/-}$ mice were isolated and cell suspensions obtained using 40-μM pore filters. Erythrocytes were lysed with AKT lysis buffer (0.15 M NH_4Cl, 10 mM $KHCO_3$, 0.1 mM EDTA), and cells were activated with the appropriate OVA peptide for 3 days. Antigen was removed, and cells were cultured with IL-2 (5 ng/ml) or IL-15 (20 ng/ml). For some experiments, naïve OT-I and OT-II cells were obtained by negative selection using the Dynabeads Untouched Mouse CD4 Cell Kit (Thermo Fisher). Flow cytometry indicated > 85% enrichment in all cases. Memory $CD4^+$ T cells, generated *in vivo* after NIP-OVA or NIP-KLH immunization (see below), were isolated by negative selection with the Mouse Memory T cell $CD4^+/CD62L^-/CD44^{hi}$ Column Kit (R&D Systems).

Blood samples from *ccr5*Δ32 homozygous and WT healthy donors were from the Fundació ACE (Barcelona, Spain) and obtained with informed consent of the donors. No personal data were registered, and all procedures using these samples were in accordance with the standards approved by the Ethics Committee of the Hospital Clinic Barcelona (HCB/2014/0494 and HCB/2016/0659). Human peripheral blood mononuclear cells (PBMC) were isolated from Vacutainer Cell Preparation Tubes by separation on a Ficoll gradient. $CD4^+$ T cells were obtained by negative selection using the EasySep Human $CD4^+$ Enrichment kit (Stem Cell Technologies) and stimulated with anti-CD3-coated magnetic beads (Dynabeads M-450 tosyl-activated, Thermo Fisher) for 3 days. Beads were removed with a magnet, and cells were incubated with IL-2 (5 ng/ml) to generate lymphoblasts. The *ccr5*Δ32 polymorphism (rs333) was genotyped by PCR (AriaMx Real-time; Agilent Technologies) as described (Mañes *et al*, 2003).

Flow cytometry

For cell surface markers, cell suspensions were incubated (20 min, 4°C) with the indicated fluorochrome-labeled or biotinylated monoclonal primary antibodies in phosphate-buffered saline with 1% BSA and 0.02% NaN_3 (PBS staining buffer). For intracellular labeling, cells were fixed and permeabilized with IntraPrep (Beckman Coulter), followed by intracellular staining with indicated antibodies. Cells were analyzed on Cytomics FC500 or Gallios cytometers (both from Beckman Coulter) and data analyzed using FlowJo software.

Immunization and adoptive transfer

Spleen and lymph node cell suspensions from OT-II WT or $CCR5^{-/-}$ cells were adoptively transferred (5×10^6 cells/mouse) into CD45.1 mice. The following day, recipient mice were infected intravenously with rVACV-OVA virus (2×10^6 pfu). Mice were sacrificed 35 days later, and splenocyte suspensions were obtained as described above.

C57BL/6J or $CCR5^{-/-}$ mice were immunized (i.p.) with NIP-OVA (200 μg) in alum (100 μl) diluted 1:1 in PBS. At 7 days post-immunization, spleens from three mice of each genotype were harvested and analyzed by flow cytometry to detect T_{fh} cells. On day 30, mice were randomized in a blind manner and half of the mice in each group were re-immunized with NIP-OVA/alum (as above); the other half received NIP-KLH (200 μg)/alum. Mice were sacrificed 15 days later, and serum anti-NIP antibodies were determined by ELISA. Plate-bound NP(7)-BSA and NP(41)-BSA (5 μg/ml) were used to measure high- and low-affinity Ig, respectively. Sera from NIP-OVA- and NIP-KLH-immunized mice were diluted 1:175, and, after several washing steps, anti-NIP antibody binding was developed with the SBA Clonotyping System-HRP (Southern Biotech). Absorbance at 405 nm was determined in a FilterMax F5 microplate reader (Molecular Devices). Memory cells from NIP-OVA- and NIP-KLH-immunized mice were purified as indicated and processed for EM.

Immunogold labeling, replica preparation, and EM analysis

Immunogold-labeled cell surface replicas were obtained as described (Kumar *et al*, 2011). Briefly, T cells were fixed in 1% paraformaldehyde (PFA) and labeled with anti-mouse CD3 mAb (145-2C11) or anti-human CD3 mAb OKT3, followed by 10 nm gold-conjugated protein A (Sigma-Aldrich). Labeled cells were adhered to poly-L-lysine-coated mica strips and fixed with 0.1% glutaraldehyde. Samples were covered with another mica strip, frozen in liquid ethane (KF-80, Leica), and stored in liquid nitrogen. Cell replicas were prepared with a Balzers 400T freeze fracture (FF) unit, mounted on copper grids, and analyzed on a

JEM1010 electron microscope (Jeol, Japan) operating at 80 kV. Images were taken with a CCD camera (Bioscan, Gatan, Pleasanton, CA) and processed with TVIPS software (TVIPS, Gauting, DE). EM images were collected by two researchers, one of them blind to the experiment. Gold particles were counted on the computer. When distance between gold particles was smaller than their diameter (10 nm), they were considered part of the same cluster.

BN-PAGE analysis of TCR clustering

Membrane fractions from OT-II WT and CCR5$^{-/-}$ cells (20×10^6) were prepared with a Dounce homogenizer, followed by incubation in hypotonic buffer (10 mM HEPES pH 7.4, 42 mM KCl, 5 mM $MgCl_2$, protease inhibitors). Membranes were recovered by ultracentrifugation (100,000 *g*, 45 min, 4°C) and lysed in 150 µl BN lysis buffer (500 mM Bis-Tris 40 mM pH 7.0, 1 mM ε-aminocaproic acid, 40 mM NaCl, 20% glycerol, 4 mM EDTA, and 0.5% Brij96 or 1% digitonin) with protease inhibitors. BN-PAGE gradient gels (4–8%) were prepared and used as described (Swamy & Schamel, 2009), using ferritin 24-mer and 48-mer (f1, 440 kDa; f2, 880 kDa) as protein markers. Proteins were transferred to PVDF membranes and probed with anti-CD3ζ antibody.

Restimulation assays

Splenocytes from CD3ε$^{-/-}$ mice were irradiated (15 Gy), seeded (0.6×10^5 cells/well), and loaded (2 h, 37°C) with different concentrations of $OVA_{323–339}$ peptide. After centrifugation (300 *g*, 5 min), isolated lymphoblasts (0.75×10^5 cells/well) were co-cultured for 48 h. Supernatants were collected to measure IL-2 by ELISA (ELISA MAX Deluxe, BioLegend) and proliferation was assessed by methyl-^{3}[H]-thymidine (1 µCi/well) incorporation into DNA, in a 1450 Microbeta liquid scintillation counter (PerkinElmer).

TCR purification

The TCR fused to streptavidin-binding peptide was purified from M.mζ-SBP cells. Briefly, 100×10^6 cells were lysed in lysis buffer (20 mM Bis-Tris pH 7, 500 mM ζ-aminocaproic acid, 20 mM NaCl, 2 mM EDTA, 10% glycerol, 1% digitonin). After incubation of the lysate with streptavidin-conjugated agarose (overnight, 4°C), the TCR was eluted by incubating samples with 2 mM biotin in lysis buffer (30 min, 4°C).

Preparation of large unilamellar vesicles and TCR reconstitution

Large unilamellar vesicles with a custom lipid composition were prepared by the thin film method (Molnar *et al*, 2012), followed by extrusion through polycarbonate membranes with a pore size of 200 nm (21 times) and 80 nm (51 times). The diameter of the resulting LUV was determined by dynamic light scattering (Zetamaster S, Malvern Instruments). The LUV preparation (2 mM) was mixed with purified TCR (0.1 µg) in 100 µl saline-phosphate buffer with 0.02% Triton X-100, and 40 µl 0.01% Triton X-100 was added. Samples were agitated (30 min, 4°C), and detergent was removed by adsorption to polystyrene Bio-Beads SM-2 (3 mg; Bio-Rad; overnight, 4°C). Proteoliposomes were collected by ultracentrifugation (180,000 *g*, 4 h, 4°C), lysed, and analyzed by BN-PAGE as above.

Sphingolipid and Chol quantification

Total Chol level was measured with the Amplex Red Cholesterol Assay Kit (Invitrogen) after lysis (50 mM Tris–HCl pH 8; 150 mM NaCl, 1% NP-40). Sphingolipid determinations were performed by an external researcher blind to the experimental groups. Prior to sphingolipid quantification, calibration curves were prepared with mixtures of C12Cer, C16Cer, C18Cer, C24Cer, C24:1 Cer, C16dhCer, C18dhCer, C24dhCer, C24:1dhCer, C12SM, C16SM, C18SM, C24SM, and C24:1SM. For sphingolipid determination, cell pellets (1×10^6) were mixed with internal standards (*N*-dodecanoyl-sphingosine, *N*-dodecanoylglucosylsphingosine, *N*-dodecanoyl-sphingosylphosphorylcholine, C17-sphinganine, and C17-sphinganine-1 phosphate; 0.2 nmol each; Avanti Polar Lipids) in a methanol:chloroform solution. Sphingolipids were extracted as described (Merrill *et al*, 2005), solubilized in methanol, and analyzed by ultra-performance liquid chromatography (UPLC; Waters, Milford, MA) connected to a time-of-flight detector (TOF; LCT Premier XE) controlled by Waters/Micromass MassLynx software. Lipid species were identified based on accurate mass measurement with an error < 5 ppm, and their LC retention time was compared with the standard (± 2) (Muñoz-Olaya *et al*, 2008).

SMase treatment

All experiments (sphingolipid quantification, apoptosis, and TCR nanoclustering) were performed by incubating OT-II WT and CCR5$^{-/-}$ cells (0.2×10^6) with recombinant sphingomyelinase from *Bacillus cereus* (0.5 U/ml; 1 h, 37°C) in serum-free medium. Cells were washed and processed immediately for EM analysis or for sphingolipid quantification as above.

Quantitative RT–PCR analyses

Total RNA was extracted from human or murine cells using the RNeasy Mini Kit (Qiagen), and cDNA was synthesized from 1 µg total RNA (High Capacity cDNA Reverse Transcription Kit, Promega). Quantitative RT–PCR was performed using FluoCycle II SYBR Master Mix (EuroClone) with specific primers (Appendix Table S3) in an ABI 7300 Real-Time PCR System (Applied Biosystems). Results were analyzed using SDS2.4 software.

CerS2 silencing

Lentiviruses were produced in HEK-293T cells after co-transfection with pGIPZ-shRNA-CerS2 or control plasmids, pSPAX2 and pMD2.G (VSV-G protein) using LipoD293tm (SignaGen). Supernatants were concentrated by ultracentrifugation and supplemented with polybrene (8 µg/ml). Lymphoblasts (3 days post-activation) or 2B4 cells (1.5×10^6 cells/ml) were resuspended in lentiviral supernatant and centrifuged (900 *g*, 90 min, 37°C). Transduction efficiency was analyzed after 24 h by FACS. In the case of 2B4 cells, transduced

cells were selected with puromycin (2 μg/ml) for 3 days prior to analyses.

Immunofluorescence analyses

OT-II 10-day WT or CCR5$^{-/-}$ lymphoblasts were plated in poly-L-lysine-coated coverslips (Nunc Lab-Tek Chamber Slide, Thermo Scientific; 50 μg/ml, overnight, 4°C). After adhesion (1 h, 37°C), cells were fixed in 4% PFA (10 min), Triton-X100-permeabilized (0.3% in PBS, 15 min), and blocked with BSA 0.5% in PBS. Samples were incubated (overnight, 4°C) with anti-mouse phospho-GATA1^{pSer142} antibody (1/200), followed by anti-rabbit Ig Alexa-488 secondary antibody (1 h). Coverslips were mounted in Fluoromount-G with DAPI (Southern Biotech); images were acquired with a Zeiss LSM710 and analyzed by a blind observer with NIH ImageJ software.

ChIP assay

Chromatin immunoprecipitation assays were performed with the EZ-ChIP Kit (Millipore). In brief, OT-II WT or CCR5$^{-/-}$ lymphoblasts (2×10^7) were fixed (1% PFA, 10 min, RT) and quenched (125 mM glycine, 5 min, RT). Cells were harvested (1×10^7 cells/ml), lysed (15 min, 4°C), and DNA sheared by sonication (45 cycles; 30 s on/off; Bioruptor Pico, Diagenode) in aliquots (0.2 ml). Of each lysate, 1% was stored as input reference, and the remaining material was immunoprecipitated (14 h, 4°C, with rotation) with antibodies to GATA1, histone H3-Lys9, or purified IgG (control). Immune complexes were captured using Protein G Magnetic Beads (Bio-Rad) and, after washing, eluted with 100 mM $NaHCO_3$, 1% SDS; protein/DNA bonds were disrupted with proteinase K (10 μg/μl, 2 h, 62°C). DNA was purified using spin columns, and Cers2 gene promoter sequences were analyzed with specific primers (Appendix Table S3). The relative quantity of amplified product in the input and ChIP samples was calculated (Mira *et al*, 2018).

Cell migration and Ca^{2+} flux assays

OT-II WT or CCR5$^{-/-}$ lymphoblasts (10^6) were added to the upper chamber of a Transwell (3-μm pore; Corning) and allowed to migrate toward 100 nM CCL4 for 4 h. Migrating cells were quantified by flow cytometry (Cytomics FC500). Mobilization of intracellular Ca^{2+} stores after CCL4 (100 nM) stimulation was measured as reported (Gómez-Moutón *et al*, 2015).

Mathematical and Bayesian analyses

To analyze cluster size distribution, we used a standard chi-square test to compare the fraction of clusters of a given size (1, 2, 3, etc.) in each dataset. In all plots, "Random" refers to synthetic distributions of receptors generated randomly.

To quantify the mechanistic relevance of cluster size between random distributions of clusters and clusters in WT and in CCR5$^{-/-}$ CD4$^+$ T cells, we used a Bayesian inference model on top of a mechanistic model (Castro *et al*, 2014). The model assumes that TCR aggregates by incorporating one receptor at a time, with on and off rates that depend on the diffusion properties of the receptor on the membrane, but not existing cluster size. That is,

$$1 \underset{q+}{\overset{q-}{\rightleftharpoons}} 2 \underset{q+}{\overset{q-}{\rightleftharpoons}} 3 \underset{q+}{\overset{q-}{\rightleftharpoons}} \ldots \underset{q+}{\overset{q-}{\rightleftharpoons}} n-1 \underset{q+}{\overset{q-}{\rightleftharpoons}} n \underset{q+}{\overset{q-}{\rightleftharpoons}} n+1 \ldots$$

The "affinity" of the process is given by $b = q+/q-$, which we also refer to as the clustering or affinity parameter. In the steady state, we can calculate analytically the fraction of clusters of a given size n:

$$\pi_n = \frac{b^{n-1}(1-b)}{(1-b^{N_{\max}})}$$

with

$$b < 1, \quad n \epsilon \{1, 2, 3, \ldots, N_{\max}\}.$$

The model was fitted using the Bayesian JAGS code (Kruschke, 2014) (see Appendix Supplementary Methods). The histograms for the number of clusters of a given size n (N_n) were modeled as a multinomial distribution with the number of observations, N, given by the total count per experiment, and probabilities π_n given by the formulas above. The priors for the clustering parameter b are beta distributions with shape parameters A and B with non-informative uniform priors. Specifically,

$N_n \sim$ Multinomial ($\pi_{n,\,N}$)
$b \sim$ Beta (A, B)
$A \sim$ Uniform (0, 1,000)
$B \sim$ Uniform (0, 1,000)

Posterior distribution of the estimated clustering parameter, b, is given with the so-called Region of Practical Equivalent (ROPE), defined as the probability of a parameter from a dataset to be explained by another dataset. ROPE quantifies the probability that the observed clustering parameter (and distribution of clusters) in the experiment can be obtained by pure random proximity.

At the molecular level, the kinetic rates q^+ and q^- can be expressed in terms of the diffusion rates of the receptors, $k_d^{+/-}$, the receptor size (a), the mean distance between receptors (s), and the correct receptor–receptor binding rates, $k^{+/-}$, through the equations (Lauffenburger & DeLisi, 1983):

$$q+ = \frac{k_d^+ k^+}{k_d^+ + k^-} \quad q- = \frac{k_d^- k^-}{k_d^+ + k^-} \Rightarrow b = \frac{k_d^+ k^+}{k_d^- + k^-}$$

with

$$k_d^+ = \frac{4\pi D}{\log(s/a) - 3/4} \quad k_d^- = \frac{2\pi D}{s^2(\log(s/a) - 3/4)}.$$

The clustering parameter b is independent of the TCR diffusivity (as D is canceled), so the observed TCR nanoclustering differences for WT and CCR5$^{-/-}$ cells would be due to TCR-TCR interactions, as previously reported (Beck-Garcia *et al*, 2015).

Identification of transcription factors in CerS promoters

Cers2, Cers3, Cers4, and Cers6 gene coordinates were obtained from the UCSC Genome browser (https://genome.ucsc.edu/; mouse genome version GRCm38/mm10). Known transcription factors for these genes were identified at GTRD v17.04 (http://gtrd17-04.biouml.org/). Venn diagrams were constructed to identify common and specific transcription factors for ceramide synthase genes.

Statistical analyses

For comparison between two conditions, data were analyzed using parametric Student's *t*-tests, paired when different treatments were applied to the same sample, or unpaired with Welch's correction. Multiple parametric comparisons were analyzed with one-way ANOVA with Bonferroni's *post-hoc* test. The chi-square test was used to analyze overall distribution of gold particles. F test was used to compare variances. All analyses were performed using Prism 6.0 or 7.0 software (GraphPad). Differences were considered significant when $P < 0.05$.

Data and code availability

This study includes no data deposited in external repositories. The authors confirm that all relevant data and materials supporting the findings of this study are available on reasonable request. This excludes materials obtained from other researchers, who must provide their consent for transfer. The Bayesian JAGS code generated in the study is provided as supplementary information in the Appendix Supplementary Methods.

Expanded View for this article is available online.

Acknowledgements
We thank D Sancho and JW Yewdell for rVACV-OVA virus, RM Peregil for technical assistance, MC Moreno and S Escudero for flow cytometry services (CNB), MT Rejas and M Guerra for EM service (CBM-SO), and C Mark for excellent editorial assistance. Fundació ACE would like to thank patients, controls, and the staff who participated in this project. This work was funded by grants from the Spanish Ministerio de Ciencia, Innovación y Universidades (SAF2017–83732-R to SM; FIS2016-78883-C2-2-P to MC; CTQ2017-85378-R; AEI/FEDER, EU), the Instituto de Salud Carlos III (ISCIII) (PI13/02434, PI16/01861 to AR), the Comunidad de Madrid (B2017/BMD-3733; IMMUNOTHERCAN-CM to SM), and the Merck-Salud Foundation (to SM). WWS and CD were supported by the Deutsche Forschungsgemeinschaft (DFG) through BIOSS-EXC294 and CIBSS-EXC 2189 (Project 390939984), SCHA976/7-1, and SFB1381. The Genome Research @ Fundació ACE project (GR@ACE) is supported by the Fundación Bancaria La Caixa, Grifols SA, Fundació ACE, and ISCIII (Ministry of Health, Spain). Fundació ACE is a participating center in the Dementia Genetics Spanish Consortium (DEGESCO).

Author contributions
SM conceived the study. AM-L and RB designed, performed most experiments, and interpreted data. JC and GF performed lipid analyses, and CD performed liposome experiments. ER-B performed analysis of TCR chains. MC carried out mathematical simulations and Bayesian analyses. MES carried out bioinformatic analyses. IR, LMR, and AR performed *ccr5*Δ32 genotyping and provided samples. WWAS, HMS, and BA contributed ideas and technical support. SM and RB wrote the manuscript. All authors read, discussed, and edited the manuscript.

Conflict of interest
The authors declare that they have no conflict of interest.

References

Alonso A, Goñi FM (2018) The physical properties of ceramides in membranes. *Annu Rev Biophys* 47: 633 – 654

Beck-Garcia K, Beck-Garcia E, Bohler S, Zorzin C, Sezgin E, Levental I, Alarcon B, Schamel WW (2015) Nanoclusters of the resting T cell antigen receptor (TCR) localize to non-raft domains. *Biochim Biophys Acta* 1853: 802 – 809

Bedognetti D, Spivey TL, Zhao Y, Uccellini L, Tomei S, Dudley ME, Ascierto ML, De Giorgi V, Liu Q, Delogu LG *et al* (2013) CXCR3/CCR5 pathways in metastatic melanoma patients treated with adoptive therapy and interleukin-2. *Br J Cancer* 109: 2412 – 2423

Blanpain C, Libert F, Vassart G, Parmentier M (2002) CCR5 and HIV infection. *Receptors Channels* 8: 19 – 31

Camargo JF, Quiñones MP, Mummidi S, Srinivas S, Gaitan AA, Begum K, Jimenez F, VanCompernolle S, Unutmaz D, Ahuja SS *et al* (2009) CCR5 expression levels influence NFAT translocation, IL-2 production, and subsequent signaling events during T lymphocyte activation. *J Immunol* 182: 171 – 182

Castellino F, Huang AY, Altan-Bonnet G, Stoll S, Scheinecker C, Germain RN (2006) Chemokines enhance immunity by guiding naive $CD8^+$ T cells to sites of $CD4^+$ T cell-dendritic cell interaction. *Nature* 440: 890 – 895

Castro BM, Silva LC, Fedorov A, de Almeida RF, Prieto M (2009) Cholesterol-rich fluid membranes solubilize ceramide domains: implications for the structure and dynamics of mammalian intracellular and plasma membranes. *J Biol Chem* 284: 22978 – 22987

Castro M, van Santen HM, Ferez M, Alarcon B, Lythe G, Molina-Paris C (2014) Receptor pre-clustering and T cell responses: insights into molecular mechanisms. *Front Immunol* 5: 132

Contento RL, Molon B, Boularan C, Pozzan T, Mañes S, Marullo S, Viola A (2008) CXCR4-CCR5: a couple modulating T cell functions. *Proc Natl Acad Sci USA* 105: 10101 – 10106

Crotty S (2011) Follicular helper CD4 T cells (TFH). *Annu Rev Immunol* 29: 621 – 663

Dawson TC, Beck MA, Kuziel WA, Henderson F, Maeda N (2000) Contrasting effects of CCR5 and CCR2 deficiency in the pulmonary inflammatory response to influenza A virus. *Am J Pathol* 156: 1951 – 1959

DeJarnette JB, Sommers CL, Huang K, Woodside KJ, Emmons R, Katz K, Shores EW, Love PE (1998) Specific requirement for CD3epsilon in T cell development. *Proc Natl Acad Sci USA* 95: 14909 – 14914

Dolan MJ, Kulkarni H, Camargo JF, He W, Smith A, Anaya JM, Miura T, Hecht FM, Mamtani M, Pereyra F *et al* (2007) CCL3L1 and CCR5 influence cell-mediated immunity and affect HIV-AIDS pathogenesis via viral entry-independent mechanisms. *Nat Immunol* 8: 1324 – 1336

Ellwanger JH, Chies JAB (2019) Host immunogenetics in tick-borne encephalitis virus infection-The CCR5 crossroad. *Ticks Tick Borne Dis* 10: 729 – 741

Falcon A, Cuevas MT, Rodriguez-Frandsen A, Reyes N, Pozo F, Moreno S, Ledesma J, Martinez-Alarcon J, Nieto A, Casas I (2015) CCR5 deficiency predisposes to fatal outcome in influenza virus infection. *J Gen Virol* 96: 2074 – 2078

Floto RA, MacAry PA, Boname JM, Mien TS, Kampmann B, Hair JR, Huey OS, Houben EN, Pieters J, Day C *et al* (2006) Dendritic cell stimulation by mycobacterial Hsp70 is mediated through CCR5. *Science* 314: 454 – 458

Franciszkiewicz K, Le Floc'h A, Jalil A, Vigant F, Robert T, Vergnon I, Mackiewicz A, Benihoud K, Validire P, Chouaib S *et al* (2009) Intratumoral induction of CD103 triggers tumor-specific CTL function and CCR5-dependent T-cell retention. *Cancer Res* 69: 6249 – 6255

Fu W, Ergun A, Lu T, Hill JA, Haxhinasto S, Fassett MS, Gazit R, Adoro S, Glimcher L, Chan S *et al* (2012) A multiply redundant genetic switch 'locks in' the transcriptional signature of regulatory T cells. *Nat Immunol* 13: 972 – 980

Garcia-Arribas AB, Alonso A, Goñi FM (2016) Cholesterol interactions with ceramide and sphingomyelin. *Chem Phys Lipids* 199: 26 – 34

Gómez-Moutón C, Fischer T, Peregil RM, Jiménez-Baranda S, Stossel TP, Nakamura F, Mañes S (2015) Filamin A interaction with the CXCR4 third intracellular loop regulates endocytosis and signaling of WT and WHIM-like receptors. *Blood* 125: 1116 – 1125

González-Martín A, Gómez L, Lustgarten J, Mira E, Mañes S (2011) Maximal T cell-mediated antitumor responses rely upon CCR5 expression in both $CD4^+$ and $CD8^+$ T cells. *Cancer Res* 71: 5455 – 5466

Gonzalez-Martin A, Mira E, Mañes S (2012) CCR5 in cancer immunotherapy: more than an "attractive" receptor for T cells. *Oncoimmunology* 1: 106 – 108

Hu YS, Cang H, Lillemeier BF (2016) Superresolution imaging reveals nanometer- and micrometer-scale spatial distributions of T-cell receptors in lymph nodes. *Proc Natl Acad Sci USA* 113: 7201 – 7206

Huang J, Brameshuber M, Zeng X, Xie J, Li QJ, Chien YH, Valitutti S, Davis MM (2013) A single peptide-major histocompatibility complex ligand triggers digital cytokine secretion in CD4(+) T cells. *Immunity* 39: 846 – 857

Jung Y, Riven I, Feigelson SW, Kartvelishvily E, Tohya K, Miyasaka M, Alon R, Haran G (2016) Three-dimensional localization of T-cell receptors in relation to microvilli using a combination of superresolution microscopies. *Proc Natl Acad Sci USA* 113: E5916 – E5924

Kersh EN, Kaech SM, Onami TM, Moran M, Wherry EJ, Miceli MC, Ahmed R (2003) TCR signal transduction in antigen-specific memory CD8 T cells. *J Immunol* 170: 5455 – 5463

Kimachi K, Croft M, Grey HM (1997) The minimal number of antigen-major histocompatibility complex class II complexes required for activation of naive and primed T cells. *Eur J Immunol* 27: 3310 – 3317

Kitatani K, Idkowiak-Baldys J, Hannun YA (2008) The sphingolipid salvage pathway in ceramide metabolism and signaling. *Cell Signal* 20: 1010 – 1018

Kohlmeier JE, Miller SC, Smith J, Lu B, Gerard C, Cookenham T, Roberts AD, Woodland DL (2008) The chemokine receptor CCR5 plays a key role in the early memory $CD8^+$ T cell response to respiratory virus infections. *Immunity* 29: 101 – 113

Kruschke JK (2014) *Doing Bayesian data analysis: a tutorial with R, JAGS, and Stan*. Burlington, MA: Academic Press, Elsevier

Kumar A, Humphreys TD, Kremer KN, Bramati PS, Bradfield L, Edgar CE, Hedin KE (2006) CXCR4 physically associates with the T cell receptor to signal in T cells. *Immunity* 25: 213 – 224

Kumar R, Ferez M, Swamy M, Arechaga I, Rejas MT, Valpuesta JM, Schamel WW, Alarcon B, van Santen HM (2011) Increased sensitivity of antigen-experienced T cells through the enrichment of oligomeric T cell receptor complexes. *Immunity* 35: 375 – 387

Lauffenburger D, DeLisi C (1983) Cell surface receptors: physical chemistry and cellular regulation. *Int Rev Cytol* 84: 269 – 302

Laviad EL, Albee L, Pankova-Kholmyansky I, Epstein S, Park H, Merrill AH Jr, Futerman AH (2008) Characterization of ceramide synthase 2: tissue distribution, substrate specificity, and inhibition by sphingosine 1-phosphate. *J Biol Chem* 283: 5677 – 5684

Lee YH, Bae SC, Song GG (2013) Association between the chemokine receptor 5 delta32 polymorphism and rheumatoid arthritis: a meta-analysis. *Mod Rheumatol* 23: 304 – 310

Lillard JW Jr, Boyaka PN, Taub DD, McGhee JR (2001) RANTES potentiates antigen-specific mucosal immune responses. *J Immunol* 166: 162 – 169

Lillemeier BF, Mortelmaier MA, Forstner MB, Huppa JB, Groves JT, Davis MM (2010) TCR and Lat are expressed on separate protein islands on T cell membranes and concatenate during activation. *Nat Immunol* 11: 90 – 96

Lim JK, Murphy PM (2011) Chemokine control of West Nile virus infection. *Exp Cell Res* 317: 569 – 574

Mañes S, Lacalle RA, Gómez-Moutón C, del Real G, Mira E, Martínez A-C (2001) Membrane raft microdomains in chemokine receptor function. *Semin Immunol* 13: 147 – 157

Mañes S, Mira E, Colomer R, Montero S, Real LM, Gomez-Mouton C, Jimenez-Baranda S, Garzon A, Lacalle RA, Harshman K *et al* (2003) CCR5 expression influences the progression of human breast cancer in a p53-dependent manner. *J Exp Med* 198: 1381 – 1389

Martín-Blanco N, Blanco R, Alda-Catalinas C, Bovolenta ER, Oeste CL, Palmer E, Schamel WW, Lythe G, Molina-París C, Castro M *et al* (2018) A window of opportunity for cooperativity in the T Cell Receptor. *Nat Commun* 9: 2618

Martínez-Martín N, Risueño RM, Morreale A, Zaldivar I, Fernández-Arenas E, Herranz F, Ortiz AR, Alarcón B (2009) Cooperativity between T cell receptor complexes revealed by conformational mutants of CD3epsilon. *Sci Signal* 2: ra43

Martinez-Muñoz L, Rodriguez-Frade JM, Barroso R, Sorzano COS, Torreno-Pina JA, Santiago CA, Manzo C, Lucas P, Garcia-Cuesta EM, Gutierrez E *et al* (2018) Separating actin-dependent chemokine receptor nanoclustering from dimerization indicates a role for clustering in CXCR4 signaling and function. *Mol Cell* 70: 106 – 119.e10

Mellado M, Rodriguez-Frade JM, Vila-Coro AJ, Fernandez S, Martin de Ana A, Jones DR, Toran JL, Martinez A-C (2001) Chemokine receptor homo- or heterodimerization activates distinct signaling pathways. *EMBO J* 20: 2497 – 2507

Merrill AH Jr, Sullards MC, Allegood JC, Kelly S, Wang E (2005) Sphingolipidomics: high-throughput, structure-specific, and quantitative analysis of sphingolipids by liquid chromatography tandem mass spectrometry. *Methods* 36: 207 – 224

Mira E, Carmona-Rodriguez L, Perez-Villamil B, Casas J, Fernandez-Acenero MJ, Martinez-Rey D, Martin-Gonzalez P, Heras-Murillo I, Paz-Cabezas M, Tardaguila M *et al* (2018) SOD3 improves the tumor response to chemotherapy by stabilizing endothelial HIF-2alpha. *Nat Commun* 9: 575

Molnar E, Swamy M, Holzer M, Beck-Garcia K, Worch R, Thiele C, Guigas G, Boye K, Luescher IF, Schwille P *et al* (2012) Cholesterol and sphingomyelin drive ligand-independent T-cell antigen receptor nanoclustering. *J Biol Chem* 287: 42664 – 42674

Molon B, Gri G, Bettella M, Gomez-Mouton C, Lanzavecchia A, Martinez AC, Mañes S, Viola A (2005) T cell costimulation by chemokine receptors. *Nat Immunol* 6: 465 – 471

Muñoz-Olaya JM, Matabosch X, Bedia C, Egido-Gabas M, Casas J, Llebaria A, Delgado A, Fabriás G (2008) Synthesis and biological activity of a novel inhibitor of dihydroceramide desaturase. *ChemMedChem* 3: 946 – 953

Nesbeth YC, Martinez DG, Toraya S, Scarlett UK, Cubillos-Ruiz JR, Rutkowski MR, Conejo-Garcia JR (2010) $CD4^+$ T cells elicit host immune

responses to MHC class II-negative ovarian cancer through CCL5 secretion and CD40-mediated licensing of dendritic cells. *J Immunol* 184: 5654 – 5662

Nie C, Sato K, Misawa N, Kitayama H, Fujino H, Hiramatsu H, Heike T, Nakahata T, Tanaka Y, Ito M *et al* (2009) Selective infection of $CD4^+$ effector memory T lymphocytes leads to preferential depletion of memory T lymphocytes in R5 HIV-1-infected humanized NOD/SCID/IL-2Rgammanull mice. *Virology* 394: 64 – 72

Pageon SV, Tabarin T, Yamamoto Y, Ma Y, Nicovich PR, Bridgeman JS, Cohnen A, Benzing C, Gao Y, Crowther MD *et al* (2016) Functional role of T-cell receptor nanoclusters in signal initiation and antigen discrimination. *Proc Natl Acad Sci USA* 113: E5454 – E5463

Ramstedt B, Slotte JP (2002) Membrane properties of sphingomyelins. *FEBS Lett* 531: 33 – 37

Richer MJ, Pewe LL, Hancox LS, Hartwig SM, Varga SM, Harty JT (2015) Inflammatory IL-15 is required for optimal memory T cell responses. *J Clin Invest* 125: 3477 – 3490

Schamel WW, Arechaga I, Risueno RM, van Santen HM, Cabezas P, Risco C, Valpuesta JM, Alarcon B (2005) Coexistence of multivalent and monovalent TCRs explains high sensitivity and wide range of response. *J Exp Med* 202: 493 – 503

Schamel WW, Risueño RM, Minguet S, Ortiz AR, Alarcon B (2006) A conformation- and avidity-based proofreading mechanism for the TCR-CD3 complex. *Trends Immunol* 27: 176 – 182

Schamel WW, Alarcon B (2013) Organization of the resting TCR in nanoscale oligomers. *Immunol Rev* 251: 13 – 20

Schauren JS, Marasca JA, Veit TD, Monticielo OA, Xavier RM, Brenol JC, Chies JA (2013) CCR5delta32 in systemic lupus erythematosus: implications for disease susceptibility and outcome in a Brazilian population. *Lupus* 22: 802 – 809

Sherman E, Barr V, Manley S, Patterson G, Balagopalan L, Akpan I, Regan CK, Merrill RK, Sommers CL, Lippincott-Schwartz J *et al* (2011) Functional nanoscale organization of signaling molecules downstream of the T cell antigen receptor. *Immunity* 35: 705 – 720

Smith X, Schneider H, Kohler K, Liu H, Lu Y, Rudd CE (2013) The chemokine CXCL12 generates costimulatory signals in T cells to enhance phosphorylation and clustering of the adaptor protein SLP-76. *Sci Signal* 6: ra65

Sofi MH, Heinrichs J, Dany M, Nguyen H, Dai M, Bastian D, Schutt S, Wu Y, Daenthanasanmak A, Gencer S *et al* (2017) Ceramide synthesis regulates T cell activity and GVHD development. *JCI Insight* 2: e91701

Sot J, Ibarguren M, Busto JV, Montes LR, Goni FM, Alonso A (2008) Cholesterol displacement by ceramide in sphingomyelin-containing liquid-ordered domains, and generation of gel regions in giant lipidic vesicles. *FEBS Lett* 582: 3230 – 3236

Stiban J, Perera M (2015) Very long chain ceramides interfere with C16-ceramide-induced channel formation: a plausible mechanism for regulating the initiation of intrinsic apoptosis. *Biochim Biophys Acta* 1848: 561 – 567

Sundrud MS, Vancompernolle SE, Eger KA, Bruno TC, Subramaniam A, Mummidi S, Ahuja SK, Unutmaz D (2005) Transcription factor GATA-1 potently represses the expression of the HIV-1 coreceptor CCR5 in human T cells and dendritic cells. *Blood* 106: 3440 – 3448

Swamy M, Schamel WW (2009) Purification of the T cell antigen receptor and analysis by blue-native PAGE. *Methods Mol Biol* 514: 135 – 150

Toson B, Dos Santos EJ, Adelino JE, Sandrin-Garcia P, Crovella S, Louzada-Junior P, Oliveira RD, Pedroza LS, de Fatima Lobato Cunha Sauma M, de Lima CP *et al* (2017) CCR5Delta32 and the genetic susceptibility to rheumatoid arthritis in admixed populations: a multicentre study. *Rheumatology (Oxford)* 56: 495 – 497

Ugurel S, Schrama D, Keller G, Schadendorf D, Brocker EB, Houben R, Zapatka M, Fink W, Kaufman HL, Becker JC (2008) Impact of the CCR5 gene polymorphism on the survival of metastatic melanoma patients receiving immunotherapy. *Cancer Immunol Immunother* 57: 685 – 691

Vangelista L, Vento S (2017) The expanding therapeutic perspective of CCR5 blockade. *Front Immunol* 8: 1981

Vieira CR, Muñoz-Olaya JM, Sot J, Jimenez-Baranda S, Izquierdo-Useros N, Abad JL, Apellaniz B, Delgado R, Martinez-Picado J, Alonso A *et al* (2010) Dihydrosphingomyelin impairs HIV-1 infection by rigidifying liquid-ordered membrane domains. *Chem Biol* 17: 766 – 775

Vinuesa CG, Linterman MA, Yu D, MacLennan IC (2016) Follicular helper T cells. *Annu Rev Immunol* 34: 335 – 368

Wang F, Beck-Garcia K, Zorzin C, Schamel WW, Davis MM (2016) Inhibition of T cell receptor signaling by cholesterol sulfate, a naturally occurring derivative of membrane cholesterol. *Nat Immunol* 17: 844 – 850

Xu Y, Phetsouphanh C, Suzuki K, Aggrawal A, Graff-Dubois S, Roche M, Bailey M, Alcantara S, Cashin K, Sivasubramaniam R *et al* (2017) HIV-1 and SIV predominantly use CCR5 expressed on a precursor population to establish infection in T follicular helper cells. *Front Immunol* 8: 376

CCR5 deficiency impairs CD4$^+$ T cell memory responses and antigenic sensitivity through increased ceramide synthesis

Ana Martín-Leal, Raquel Blanco, Josefina Casas, María E. Sáez, Elena Rodríguez-Bovolenta, Itziar de Rojas, Carina Drechsler, Luis Miguel Real, Gemma Fabrias, Agustín Ruíz, Mario Castro, Wolfgang W.A. Schamel, Balbino Alarcón, Hisse M. van Santen, Santos Mañes

Supplemental information

Appendix Figure S1 – S8

Appendix Tables S1 – S3

Bayesian code

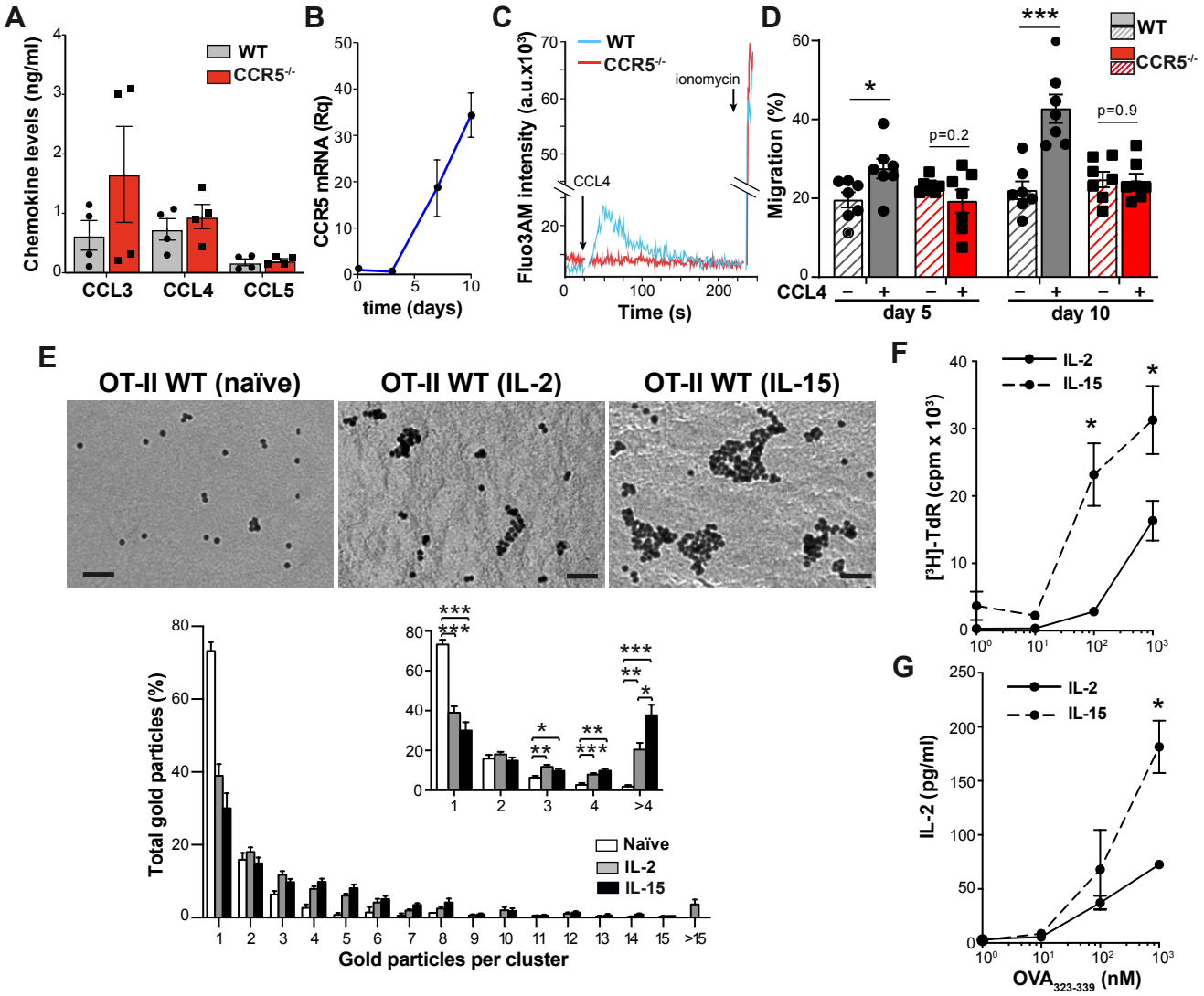

Appendix Figure S1. Characterization of CD4⁺ T lymphoblasts. A. CCR5 ligand levels in supernatants of day 10 IL-2-expanded OT-II WT and CCR5$^{-/-}$ lymphoblasts. Data shown as mean ± SEM (n = 4). **B.** Relative CCR5 mRNA levels in OT-II WT lymphoblasts. mRNA was not detected in OT-II CCR5$^{-/-}$ lymphoblasts. **C.** Time course of intracellular Ca^{2+} mobilization in response to CCL4 in OT-II WT and CCR5$^{-/-}$ lymphoblasts. Cells were finally treated with ionomycin as a positive control of Ca^{2+} loading (n = 3). **D.** Analysis of OT-II WT and CCR5$^{-/-}$ lymphoblast transmigration in transwell chambers, using CCL4 as chemoattractant (solid bars) or in basal medium (dashed bars). Data are the percentage of migrating cells relative to total cells seeded. **E.** EM analysis of TCR nanoclustering in OT-II WT naïve cells and lymphoblasts expanded in IL-2 or IL-15. Top, representative small field images showing gold particle distribution in the cell surface replicas of anti-CD3ε-labeled cells. Bottom, quantification (mean ± SEM) of gold particles in clusters of the indicated size in the IL-2- (gray bars; n = 6 cells, 27518 particles) and IL-15-expanded lymphoblasts (black; n = 8 cells, 27518 particles). Insets show the distribution between clusters of one, two, three, four or more than four particles, and statistical analysis. **F, G.** IL-2- and IL-15-expanded OT-II WT lymphoblasts were restimulated with the indicated concentrations of $OVA_{323-339}$; cell proliferation measured by thymidine incorporation into DNA (*F*) and IL-2 production measured by ELISA (*G*) were determined after 72 h of stimulation. Data shown as mean ± SEM (n = 5). * p <0.05, ** p <001, *** p <0.001, two-tailed unpaired Student's t-test. Bar, 50 nm.

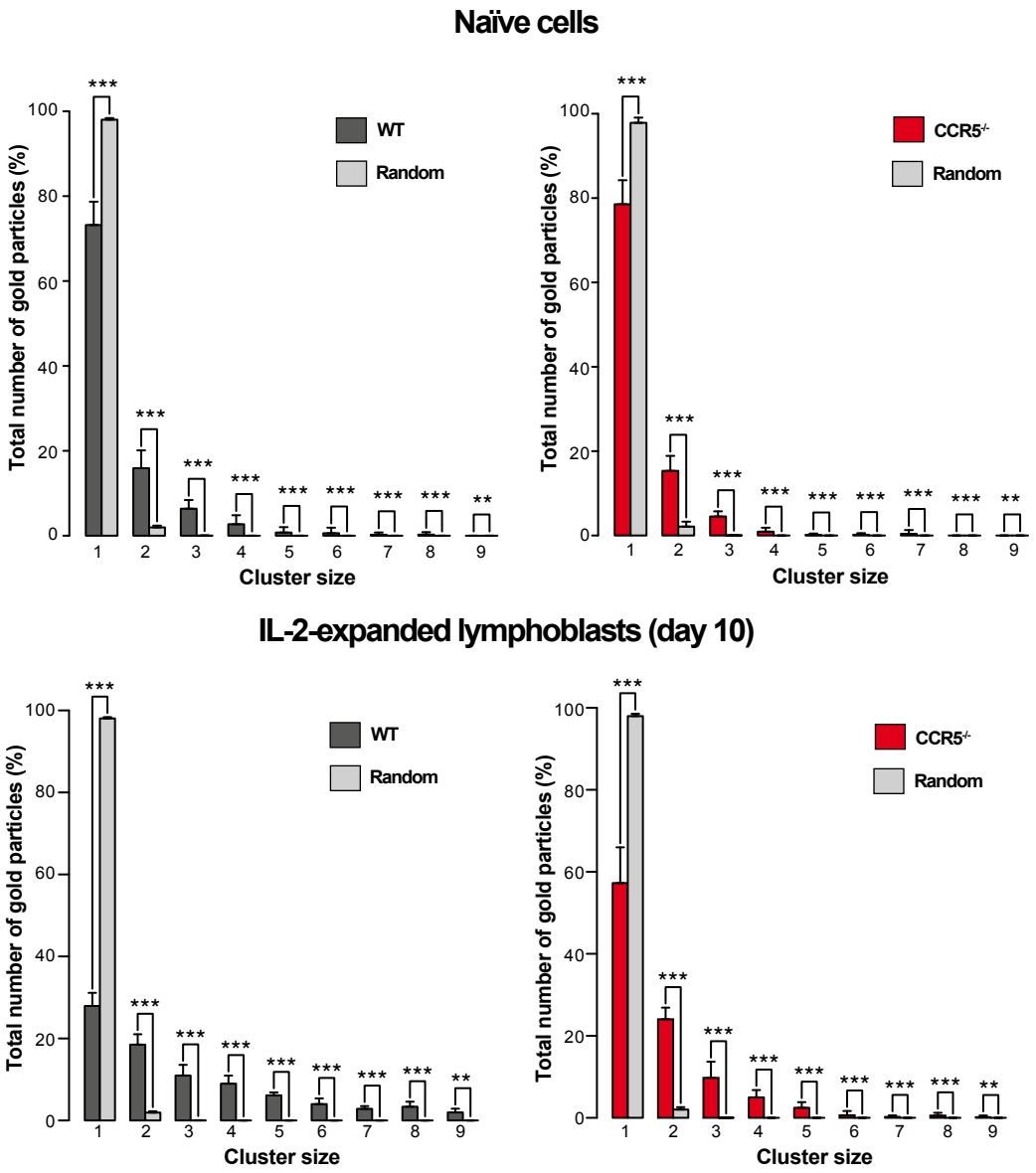

Appendix Figure S2. Comparison of experimental and synthetic TCR multimer distributions. Percentage of clusters of size *n* (1 to 9) in WT and CCR5$^{-/-}$ OT-II naïve cells and lymphoblasts (day 10) determined experimentally (dark bars), and synthetically random generated receptors (light bars). Student's *t*-test significance for each cluster size is shown above bars (p >0.05 (not significant), * p <0.05, **p <0.01, *** p <0.001). In all cases, the experimental distributions of clusters differ significantly from random proximity between clusters.

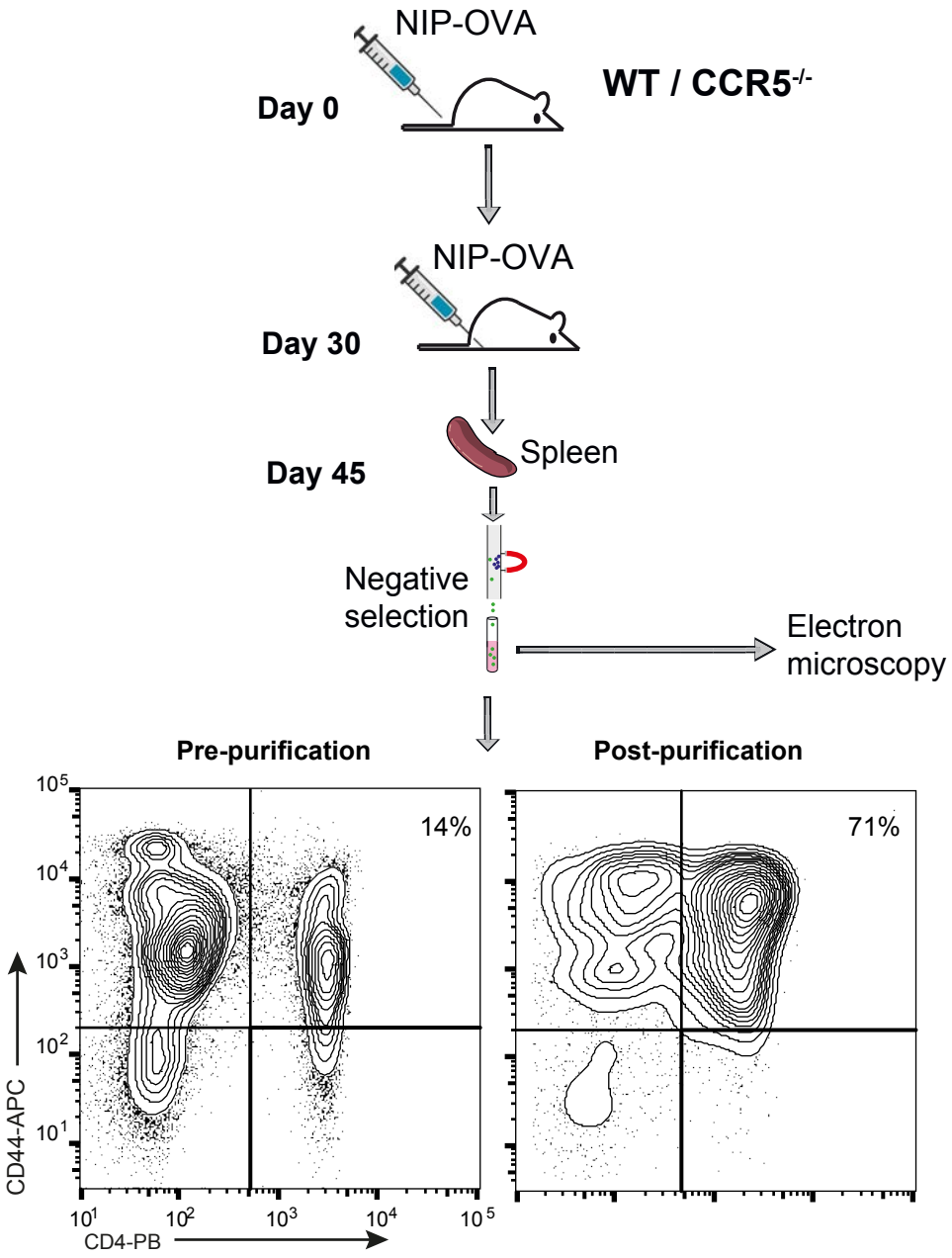

Appendix Figure S3. Characterization of endogenous memory CD4⁺ T cells uses for electron microscopy studies. Scheme of the purification of memory cells from OVA/OVA-immunized mice as well as a representative plot showing the characterization of the purified cells by flow cytometry.

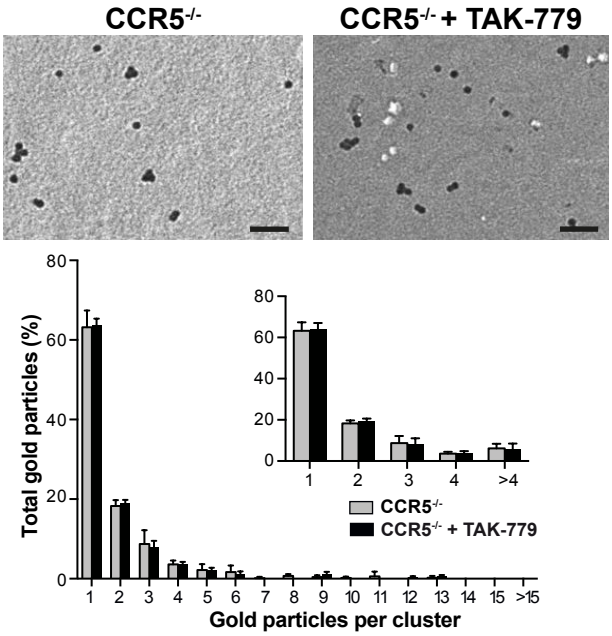

Appendix Figure S4. TAK-779 does not affect TCR nanoclustering in CCR5$^{-/-}$ lymphoblasts. OT-II CCR5$^{-/-}$ cells were activated with $OVA_{323-339}$ for 3 days in the presence of TAK-779, and lymphoblasts were generated by expansion with IL-2. Top, representative small field images showing gold particle distribution in cell surface replicas of anti-CD3ε-labeled cells. Bottom, quantification (mean ± SEM) of gold particles in clusters of the indicated size in vehicle-treated (gray bars; $n = 6$ cells, 5138 particles) and TAK-779-treated lymphoblasts (black; $n = 5$ cells, 4215 particles). Insets, distribution between clusters of one, two, three, four or more than four particles, and statistical analysis. * $p < 0.05$, one-tailed unpaired Student's *t*-test. Bar, 50 nm.

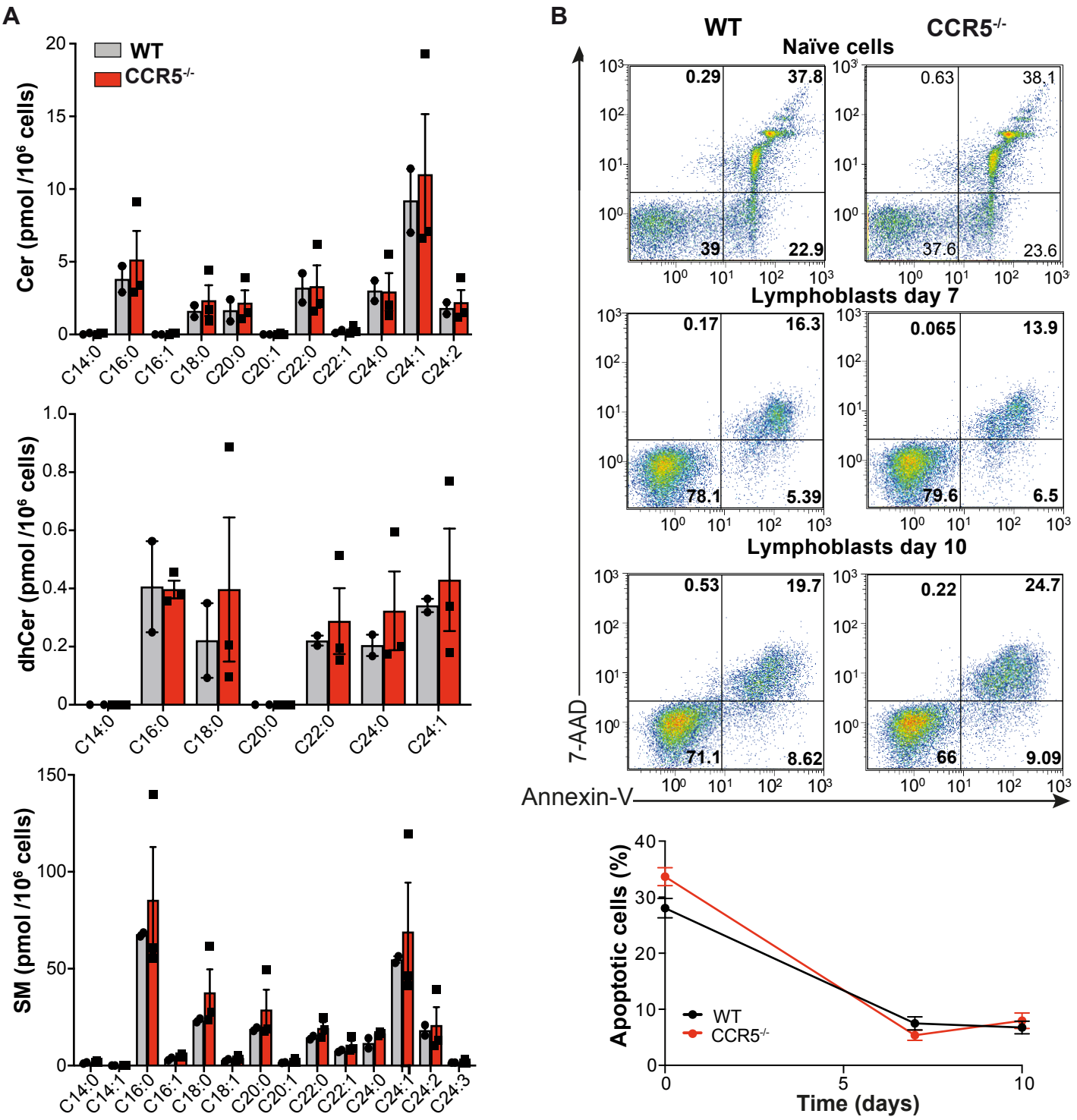

Appendix Figure S5. Analysis of sphingolipids and apoptosis in WT and CCR5$^{-/-}$ naïve OT-II cells. A. Cer (top), dhCer (center) and SM (bottom) levels in WT and CCR5$^{-/-}$ OT-II naïve cells. Values were normalized to the C17 standards and to cell number in each sample (n = 4). No significant differences were found between genotypes in any lipid species (two-tailed unpaired Student's t-test). **B.** Representative dot plots of WT and CCR5$^{-/-}$ OT-II naïve cells and IL-2 lymphoblasts at days 7 and 10, stained for the apoptosis markers 7-aminoactinomycin D (7-AAD) and annexin-V. Numbers represent the percentage of cells. The graph shows the quantification of doubled-stained cells in different experiments (bottom). Data are mean ± SEM (n = 4). No differences were found between genotypes (two-tailed unpaired Student's t-test).

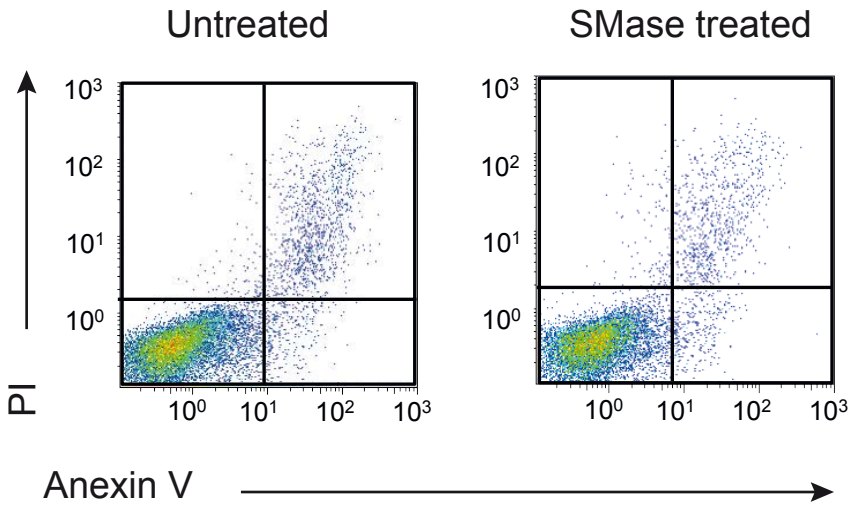

Appendix Figure S6. SMase treatment does not trigger apoptosis in lympholasts. Day 10 OT-II lymphoblasts were treated with SMase (0.5 U/ml, 1 h, 37ºC) and apoptosis determined by FACS analysis after staining with annexin-V and propidium iodide (PI). Plots shown for untreated (left) and SMase-treated cells (right) in a representative experiment (n = 4).

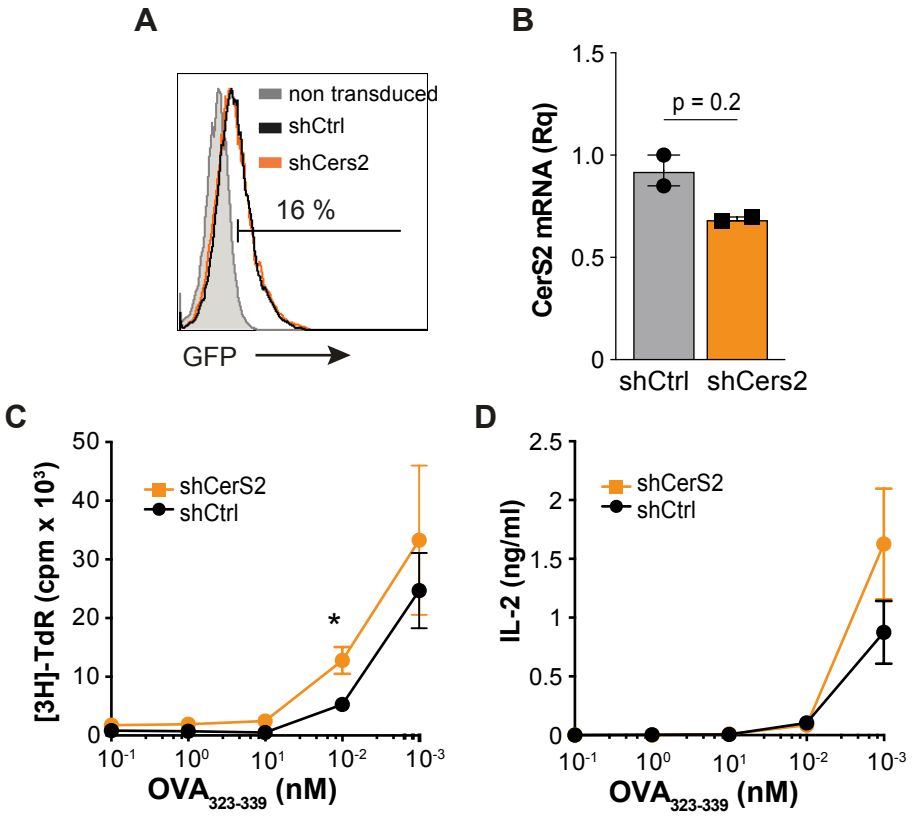

Appendix Figure S7. CerS2 silencing in primary CD4⁺ lymphoblasts. A. Histograms showing GFP staining in shCtrl- (black line) and shCerS2-transduced OT-II CCR5$^{-/-}$ lymphoblasts (orange). Data for cells stained at 72 h post-transduction in a representative experiment. Gray area represents staining of non-transduced cells (negative control). The percentage of GFP^{+} cells is indicated. **B.** Relative CerS2 mRNA levels in cells as in *A*. **C, D.** Determination of thymidine incorporation into DNA (*C*) and IL-2 levels (*D*) in the supernatant of shCtrl- (black line) and shCerS2-transduced (orange line) OT-II CCR5$^{-/-}$ lymphoblasts restimulated for 48 h with $OVA_{323-339}$ at the indicated concentrations. For *B-D*, data shown as mean ± SEM (n = 3). * $p < 0.05$, two-tailed unpaired Student's *t*-test.

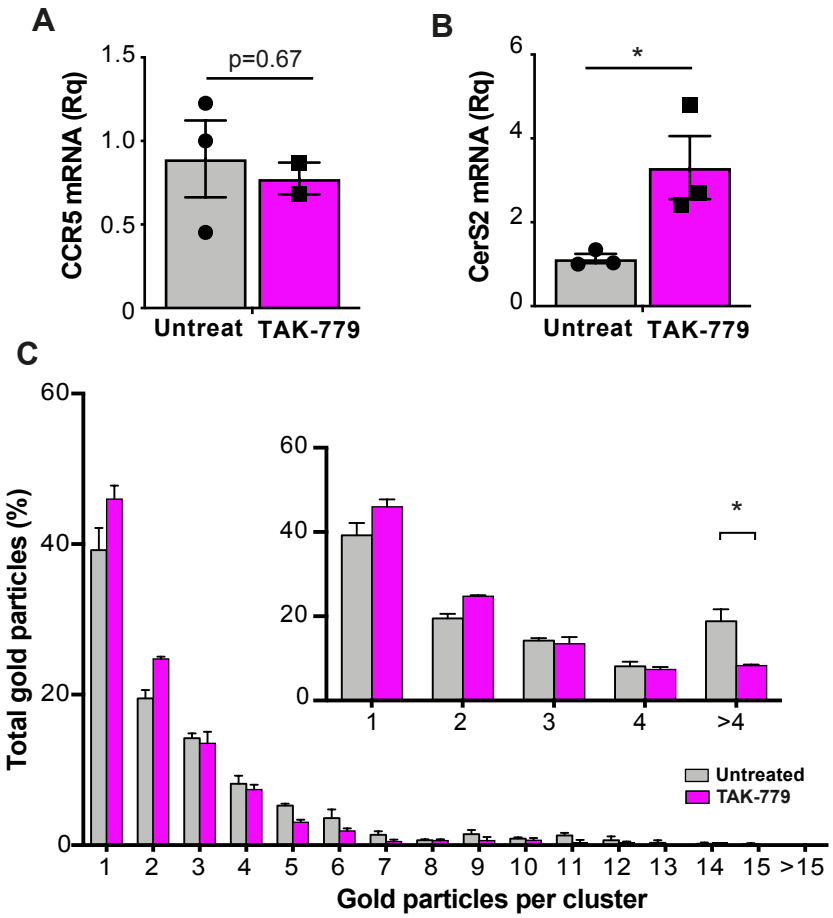

Appendix Figure S8. CCR5 blockade also impairs TCR nanoclustering in the CD4⁺ T cell hybridoma 2B4. A, B. Relative mRNA levels of CCR5 (*A*) and CerS2 (*B*) in CD3ε-activated 2B4 cells untreated (gray bars) or TAK-779-treated (10 μM; pink). **C.** Quantification (mean ± SEM) of gold particles in clusters of the indicated size in cell surface replicas of anti-CD3ε-labeled untreated (gray bars; n = 5 cells, 13266 particles) and TAK-779-treated 2B4 cells (black; n = 6 cells, 17654 particles). Insets show the distribution between clusters of one, two, three, four or more than four particles, and statistical analysis. * p <0.05, one-tailed unpaired Student's t-test.

Appendix Table S1. Number of TCR nanoclusters/cell in the different experiments

Experiment	Cell type	Genotype or treatment	TCR nanoclusters/cell	*n*
Fig. 3A	Naïve OT-II cells	WT	68.3 ± 13.25	6
		$CCR5^{-/-}$	54 ± 6.7	6
Fig. 3B	IL-2-expanded OT-II lymphoblasts	WT	379.9 ± 49.1	8
		$CCR5^{-/-}$	163.3 ± 36	6
Fig. 3C	IL-15-expanded OT-II lymphoblasts	WT	600.9 ± 47.3	8
		$CCR5^{-/-}$	364 ± 53.6	7
Fig. 3G	Purified memory $CD4^+$ T cells	WT	494.5 ± 84.9	5
		$CCR5^{-/-}$	351.4 ± 47.3	7
Fig. 4A	IL-2-expanded OT-II lymphoblasts	Medium	323.1 ± 58.5	5
		TAK-779	142.5 ± 22.3	6
Fig. 4B	IL-2-expanded OT-II lymphoblasts	Medium	211.5 ± 53.1	5
		TAK-779	195,6 ± 20,3	6
Fig. 4C	IL-2-expanded OT-II lymphoblasts	Vehicle	309.6 ± 65.9	6
		AMD3100	378.7 ± 74.5	7
Fig. 6E	IL-2-expanded OT-II lymphoblasts	Untreated	234.1 ± 58.1	5
		SMase-treated	208.5 ± 19.1	6
Fig. 6I	2B4 transduced cells	shCtrl	90.2 ± 16.5	6
		shCerS2	216 ± 63.7	7
Fig. 7A	Human $CD4^+$ T cell lymphoblasts	WT	539.9 ± 80.4	5
		ccr5Δ32	337.7 ± 172	4

Nanoclusters are defined as aggregates of gold particles >2. *n*, number of cells analyzed. Data are mean ± SEM.

Appendix Table S2. RRID accession number and catalog reference of the reagents

REAGENT	SOURCE	IDENTIFIER
Antibodies		
Anti-mouse Vα2TCR-PE (B20.1)	BD-Biosciences	Cat# 553289, RRID:AB 394760
Anti-mouse CD25-PE (PC61)	BD-Biosciences	Cat# 553866, RRID:AB 395101
Anti-mouse CD45.2-FITC (104)	BD-Biosciences	Cat# 561874,RRID:AB 10894189
Anti-mouse CD62L-FITC (MEL-14)	BD-Biosciences	Cat# 553150,RRID:AB 394665
Anti-mouse CD62L-APC (MEL-14)	BD-Biosciences	Cat# 553152,RRID:AB 398533
Anti-mouse CD69-PeCy7 (H1.2F3)	BD-Biosciences	Cat# 552879,RRID:AB 394508
Anti-mouse CXCR5 biotinylated (2G8)	BD-Biosciences	Cat# 551960,RRID:AB 394301
Anti-mouse biotin CD3ε (145-2C11)	BD-Biosciences	Cat# 553239,RRID:AB 394728
Anti-mouse unlabeled CD3ε (145-2C11)	BD-Biosciences	Cat# 553057,RRID:AB_394590
Anti-human biotin CD3 (OKT3)	Thermo Fisher Scientific	Cat# 13-0037-80, RRID:AB_1234956
Anti-mouse CD4-PeCy7 (RM4.5)	Thermo Fisher Scientific	Cat# 25-0042-81, RRID:AB_469577
Anti-mouse CD4-efluor450 (RM4.5)	Thermo Fisher Scientific	Cat# 48-0042-80, RRID:AB_1272231
Anti-mouse CD4-PacificBlue (RM4.5)	Thermo Fisher Scientific	Cat# MCD0428, RRID:AB_10372505
Anti-mouse IFNγ-APC (XMG1.2)	Thermo Fisher Scientific	Cat# 17-7311-82, RRID:AB_469504
Anti-mouse PD1-efluor780 (J43)	Thermo Fisher Scientific	Cat# 47-9985-82, RRID:AB_2574002
Anti-mouse phospho-GATA1-pSer142	Thermo Fisher Scientific	Cat# PA5-37581, RRID:AB_2554189
Anti-mouse CD44-Pe/Cy5 (IM7)	BioLegend	Cat# 103009, RRID:AB_312960
Anti-mouse CD44-APC (IM7)	BioLegend	Cat# 103011, RRID:AB_312962
Anti-mouse CerS2 (1A6)	Novus Biologicals	Cat# H00029956-M01A, RRID:AB_2132954
Anti-mouse CerS3 (6C12)	Novus Biologicals	Cat# H00204219-M02
Anti-mouse CerS6	Novus Biologicals	Cat# H00253782-M01, RRID:AB_2133107
Anti-mouse CerS4 (polyclonal)	Sigma-Aldrich	Cat# SAB4503164, RRID:AB_10746317
Anti-mouse CD3ζ (449)	Purified from hybridoma, this study	N/A
Anti-mouse β-actin (AC-15)	Sigma-Aldrich	Cat# A1978, RRID:AB_476692
Anti-mouse GATA1 (ab11852)	Abcam	Cat# ab11852, RRID:AB_298635
Anti-acetyl histone H3Lys9 (CS200583)	EMD-Millipore	Cat# 07-352, RRID:AB_310544
purified IgG rabbit (PP64)	EMD-Millipore	Cat# PP64, RRID:AB_97852
Virus strains		
rVACV-OVA virus	a gift of J.W.Yewdell; NIH, Bethesda, MD	N/A
Biological Samples		
Healthy adult blood samples	Fundació ACE (Barcelona, Spain)	NA
Chemicals, peptides, recombinant proteins		
OVA(323–339) peptide	CNB Peptide facility	N/A
Sphingomyelinase (Bacillus cereus)	Sigma-Aldrich	Cat# S7651
TAK-779	Sigma-Aldrich	Cat# SML0911
AMD-3100	Sigma-Aldrich	Cat# 239820
poly-L-lysine	Sigma-Aldrich	Cat# P4707

Ceramide (bovine spinal cord)	Sigma-Aldrich	Cat# 22244
Protein A-Gold	Sigma Aldrich	Cat# P6730
Streptavidin-agarose	Sigma Aldrich	Cat# S1638
Ceramide from bovine spinal cord	Sigma Aldrich	Cat# 22244
NIP-OVA	Biosearch Technologies	Cat# N-5041
NIP-KLH	Biosearch Technologies	Cat# N-5042
Aluminium hydroxide gel	InvivoGen	Cat# vac-alu-250
Streptavidin APC	Thermo Fisher Scientific	Cat# 17-4317-82
Streptavidin PerCP-Cy5	Thermo Fisher Scientific	Cat# 45-4317-82; RRID: AB_10311495
Dynabeads™ M-450 Tosylactivated	Thermo Fisher Scientific	Cat# 14013
Proteinase K	Thermo Fisher Scientific	Cat# 25530049
Streptavidin BV786	BD Bioscience	Cat# 563858
Recombinant murine CCL4	PeproTech	Cat# 250-32
Recombinant murine IL-2	PeproTech	Cat# 212-12
Recombinant murine IL-15	PeproTech	Cat# 210-15
Recombinant human IL-2	PeproTech	Cat# AF-200-02
LIVE/DEAD™ Fixable Near-IR Dead Cell Stain Kit	Molecular Probes	Cat# 10154363
DAPI Fluoromount-G	Southern Biotech	Cat# 0100-20
Thymidine, [Methyl-3H]	Pelkin Elmer	Cat# NET027W001MC
SureBeads™ Protein G Magnetic Beads	Bio Rad	Cat# 1614023
LipoD293™ In Vitro DNA Transfection Reagent	SignaGen Laboratories	Cat# SL100668
Cholesterol	Avanti Polar Lipids	Cat#700100
Soybean L-α-phosphatidylcholine	Avanti Polar Lipids	Cat#840054C
Egg Sphingomyelin	Avanti Polar Lipids	Cat#860061C
C12 Ceramide (d18:1/12:0)	Avanti Polar Lipids	Cat# 860512
C16 Ceramide (d18:1/16:0)	Avanti Polar Lipids	Cat# 860516
C18 Ceramide (d18:1/18:0)	Avanti Polar Lipids	Cat# 860518
C24 Ceramide (d18:1/24:0)	Avanti Polar Lipids	Cat# 860524
C24:1 Ceramide (d18:1/24:1(15Z))	Avanti Polar Lipids	Cat# 860525
C16 Dihydroceramide (d18:0/16:0)	Avanti Polar Lipids	Cat# 860634
C18 Dihydroceramide (d18:0/18:0)	Avanti Polar Lipids	Cat# 860627
C24 Dihydroceramide (d18:0/24:0)	Avanti Polar Lipids	Cat# 860628
C24:1 Dihydroceramide (d18:0/24:1(15Z))	Avanti Polar Lipids	Cat# 860629
12:0 SM (d18:1/12:0)	Avanti Polar Lipids	Cat# 860583
16:0 SM (d18:1/16:0)	Avanti Polar Lipids	Cat# 860584
18:0 SM (d18:1/18:0)	Avanti Polar Lipids	Cat# 860586
24:0 SM	Avanti Polar Lipids	Cat# 860592
24:1 SM	Avanti Polar Lipids	Cat# 860593
C12 Glucosyl(β) Ceramide (d18:1/12:0)	Avanti Polar Lipids	Cat# 860543
C17 sphinganine (d17:0)	Avanti Polar Lipids	Cat# 860654
C17 sphinganine-1-phosphate (d17:0)	Avanti Polar Lipids	Cat# 860655
Chloroform	JT Baker	Cat# 15588534
Water for LC-MS	JT Baker	Cat# 15568664
Methanol for LC-MS	Fisher Chemical	Cat# 15611630
Ammonium formate for LC-MS	Fisher Chemical	Cat# 11377490
Formic Acid for LC-MS	Fluka	Cat# 15671400

Critical commercial assays

ELISA MAX™ Deluxe Set Mouse IL-2	BioLegend	Cat# 431004

Mouse Memory T cell CD4+/CD62L-/CD44hi Column Kit	R&D Systems	Cat# MCD45
Dynabeads™ Untouched™ Mouse CD4 Cells Kit	ThermoFisher	Cat# 11415D
Amplex™ Red Cholesterol Assay Kit	ThermoFisher	Cat# A12216
EasySep™ Human CD4+ T Cell Enrichment Kit	StemCell	Cat# 19052
SBA Clonotyping System-HRP	SouthernBiotech	Cat# 5300-05
RNeasy Mini Kit	QIAGEN	Cat# 74104
EZ-ChIP™	Millipore	Cat# 17-371

Experimental models: Cell lines

HEK-293 T	ATCC	Cat# CRL-3216, RRID:CVCL_0063
2B4 T cell hybridoma	J. Ashwell, Bethesda	RRID:CVCL_4Z38
M.mζ-SBP	(Swamy and Schamel, 2009)	N/A

Experimental models: Organisms

B6.129P2-Ccr5tm1Kuz (CCR5$^{-/-}$)	The Jackson Laboratory	Cat# JAX:005427, RRID:IMSR_JAX:005427
C57BL/6J	The Jackson Laboratory	Cat# JAX:000664, RRID:IMSR_JAX:000664
B6.Cg-Tg(TcraTcrb)425Cbn/J (OT-II)	The Jackson Laboratory	Cat# JAX:004194, RRID:IMSR_JAX:004194)
OT-II-CCR5$^{-/-}$	(González-Martín et al., 2011)	N/A
B6.SJL-Ptprca Pepcb/Boy	The Jackson Laboratory	Cat# JAX:002014, RRID:IMSR_JAX:002014
CD3ε$^{-/-}$	(DeJarnette et al., 1998)	N/A

Oligonucleotides

Primers for qRT-PCR, see Table S1		N/A

Software and Algorithms

Bayesian JAGS code		Provided as supplementary material
FlowJo v10	Tree Star	RRID:SCR_008520
GraphPad Prism v6 & v7	GraphPad	RRID:SCR_002798
NIH Image J	NIH Image	RRID:SCR_003073
UCSC Genome browser	University of California Santa Cruz	RRID:SCR_005780
GTRD v17.04	Gene Transcription Regulation Database	http://gtrd17-04.biouml.org/
Venny 2.1	BioinfoGP, CNB/CSIC	RRID:SCR_016561
Adobe Photoshop CS5	Adobe Software	RRID:SCR_014199
Adobe Illustrator CS5	Adobe Software	RRID:SCR_010279

Others

Brefeldin A	Sigma-Aldrich	Cat# B7651
IntraPep Permeabilization reagent	Beckman Coulter	Cat# A07803
GIPZ lentiviral mouse CerS2 shRNA (clones V3LMM_454307, V3LMM_454309, V3LMM_454311)	Dharmacon	Cat# RMM4532-EG76893
Bio-Beads™ SM-2 Resin	BioRad	Cat# 1523920
Acquity C8 UPLC column	Waters	Cat# 186002878

Appendix Table S3. List of primers used for RT-qPCR analyses

Gene Symbol	Primer (5' – 3') Forward	Reverse
mCerS2	GGCGCTAGAAGTGGGAAAC	TCGAATGACGAGAAAGAGCA
mCerS3	GCTACACCTCTAGCAAATGCAC	ATCTTTCAACCTGGCGCTCT
mCerS4	AGATAAAGCCCAACCCGGTG	GTCTCCTGAACCAGCGTTGA
mCerS5	CCAATGCTGGTTTCGCCATC	AGAACCAAGGCATCGACCAG
mCerS6	GGAGCTGTCATTTTATTGGTCTTT	GGAACATAATGCCGAAGTCC
mASAH1	TGAAGATGGTGGATCAAAAGC	ACATCTGCAATTCCCCTCA
mACER2	GTGTGGCATATTCTCATCTG	TAAGGGACACCAATAAAAGC
mACER3	TGACCTTGTTCGTCGCTGAG	AGCAATGTACCGCTTCTCCA
mSMPD1	TGGTTCTGGCTCTGTTTGACTCCA	TCAGCTGATCTTGGCGAGACTGTT
mSMPD2	GGTGCTCAACGCCTATGTG	CGTCTGCCTTCTTGGATGTG
mSMPD3	AGAAACCCGGTCCTCGTACT	CCTGACCAGTGCCATTCTTT
mSMPD4	GCCAACGACCTGGACGAGATC	GCGAGTGTGAACTGCCTGAG
CCR5	TCCGTTCCCCCTACAAGAGA	TTGGCAGGGTGCTGACATAC
mTcra	CCAGACTGGCAGCAAGAAGAAAAT	TCACAGCTCCCCACCATATTC
mTcrb	GTGCTGTGAAGGATGGCAACT	CGGCAGGGTCAGGGTTCT
mCD3d	TGTGCAAGTCCATTACCGAAT	AAAGCAGTAGACGCCCAAAG
mCD3g	GAGAAGCAAAGAGACTGACATGG	TTATTTGTCTGGGCTACAGTGC
mCD3e	AACACTTTCTGGGGCATCCT	ATGTTCTCGGCATCGTCCT
mCD3z	GCACGATGGCCTTTACCA	CAAGTGACATCAGCAGGTGAA
mGATA-1	TGCTCTCTTCTTGAGGCATAGATT	CCAGCCCTGCTGTTTAGAGTC
mHISTH3	GCTAAGCTTAACTCTCCCGGT	AAGCGCCCAGCAGCC
hCerS2	GACGGAGTACACGGAGCAG	CGTTCCCACCAGAAGTAATCA
hCerS4	TGGTGCTGCTGTTACACGAT	TGATACTGCATGTAGTTGACCATC
hCerS5	CACATCCTCTCGGTGTTCC	CAGGGTTTGGCAATAAATCG
hCerS6	CGACTGGGTATATTTCCTCTCTG	GGAAGGGTAAGGTCCAACG
hASAH1	CACGCTGATTGGGTGTGTA	CGATGTTCAGCTTGTATTTCTTGA
hACER2	TGTGGTTCCCCAGAAGGTAT	ACGTCGTAACCGCAGACAG
hACER3	CCTGAGATATAGGCCAAAAGTGA	GCCAGGTCTATGGTAGGTGCT
hSMPD1	TGGCTCTATGAAGCGATGG	TGGGGAAAGAGCATAGAACC
hSMPD3	TGGTACCCAAGAACTGCTACG	AAAACCCAGAAACTGCCTTG
18S rRNA	GAGAAACGGCTACCACATCC	GGGTCGGGAGTGGGTAAT

Bayesian code for the R-language

```
# require(rjags)
# The array "p" contains 4 different cluster size counts from different
experiments for the same mouse and time
cluster.jags.multix4 <- function(p) {
  p1 <- p[1,]
  p2 <- p[2,]
  p3 <- p[3,]
  p4 <- p[4,]
  data <-
list(p1=p1,p2=p2,p3=p3,p4=p4,m=length(p1),N1=sum(p1),N2=sum(p2),N3=sum(p3),N4=su
m(p4))

  modelstring="
  model {
  for(n in 1:(m-1)) {
     pi1[n] <- b1^(n-1)*(1-b1) # Analytical distribution described in the main
text
     pi2[n] <- b2^(n-1)*(1-b2)
     pi3[n] <- b3^(n-1)*(1-b3)
     pi4[n] <- b4^(n-1)*(1-b4)
  }
  pi1[m] <- b1^(m-1)  # Analytical distribution described in the main text
  pi2[m] <- b2^(m-1)
  pi3[m] <- b3^(m-1)
  pi4[m] <- b4^(m-1)

  p1 ~ dmulti(pi1,N1) # The counts are given by a multinomial distribution with
probabilities "pi"
  p2 ~ dmulti(pi2,N2)
  p3 ~ dmulti(pi3,N3)
  p4 ~ dmulti(pi4,N4)

  b1 ~ dbeta(A,B) # Priors for the parameters b1.
  b2 ~ dbeta(A,B)
  b3 ~ dbeta(A,B)
  b4 ~ dbeta(A,B)
  A ~ dunif(0,1000) # Hyperpriors for A and B (0 = uniform distribution,
Infinity=peaked distribution)
  B ~ dunif(0,1000)
  }"

  model=jags.model(textConnection(modelstring), data=data,n.chains = 3) # Create
jags model
  update(model,n.iter=10000) # Burning phase of the MCMC model
  output=coda.samples(model=model,variable.names=c("A","B","b1","b2","b3","b4"),
n.iter=15000, thin=1) # Sample data
  print(summary(output)) # Print estimated parameters
  return(output) # return matrix of results for post-processing
}
```